

Adaptive mesh refinement for coupled elliptic-hyperbolic systems

Frans Pretorius^{a,b,*}, Matthew W. Choptuik^c

^a *CIAR Cosmology and Gravity Program, Department of Physics, P-405 Avadh Bhatia Physics Laboratory, University of Alberta, Edmonton, AB, Canada T6G 2J1*

^b *Theoretical Astrophysics 130-033, California Institute of Technology, Pasadena, CA 91125, United States*

^c *CIAR Cosmology and Gravity Program, Department of Physics and Astronomy, University of British Columbia, Vancouver, BC, Canada V6T 1Z1*

Received 20 October 2005; received in revised form 6 February 2006; accepted 7 February 2006

Available online 19 April 2006

Abstract

We present a modification to the Berger and Oligier adaptive mesh refinement algorithm designed to solve systems of coupled, non-linear, hyperbolic and elliptic partial differential equations. Such systems typically arise during constrained evolution of the field equations of general relativity. The novel aspect of this algorithm is a technique of “extrapolation and delayed solution” used to deal with the non-local nature of the solution of the elliptic equations, driven by dynamical sources, within the usual Berger and Oligier time-stepping framework. We show empirical results demonstrating the effectiveness of this technique in axisymmetric gravitational collapse simulations, and further demonstrate that the solution time scales approximately linearly with problem size. We also describe several other details of the code, including truncation error estimation using a self-shadow hierarchy, and the refinement-boundary interpolation operators that are used to help suppress spurious high-frequency solution components (“noise”).

© 2006 Elsevier Inc. All rights reserved.

Keywords: Adaptive mesh refinement; Coupled elliptic-hyperbolic systems; Finite different methods; Numerical relativity; Numerical methods

1. Introduction

Adaptive mesh refinement (AMR) will be needed for many grid-based numerical approaches designed to solve a variety of problems of interest in numerical relativity, including critical gravitational collapse, binary black hole mergers, and the study of singularity structure in cosmological settings and black hole interiors [1–3]. The reason is that such problems often exhibit a wide range of relevant spatial and temporal length scales that are impossible to adequately resolve with a uniform mesh, given resources available on contemporary

* Corresponding author. Tel.: +1 780 492 7176.

E-mail address: fransp@phys.ualberta.ca (F. Pretorius).

computers. In certain restricted scenarios, such as the head-on collision of black holes [4], or during the inspiral phase of a circular merger [5,6], it is possible to construct a single, static coordinate grid that can resolve all of the length scales. However, this requires some a priori knowledge of the structure of the solution that will not be available in general. To date, in numerical relativity, mesh refinement has been used quite effectively in 1D and 2D critical collapse simulations [7–14], the study of critical phenomena in the non-linear sigma model in 3D Minkowski space [15], in 2D simulations of cosmological spacetimes [16], 3D simulation of gravitational waves and single black holes [17–22], to construct initial data for binary black hole mergers [23–25], and the evolution of binary black hole spacetimes [5,26].¹

In the following we only consider Cauchy evolution; in other words, we have a timelike coordinate t that foliates the spacetime into a set of spacelike slices, and, given initial data at $t = 0$, we want to evolve to the future $t > 0$. In such a coordinate basis the field equations of general relativity consist of a set of 10, second order, quasi-linear partial differential equations (PDEs) for 10 metric coefficients that describe the structure of spacetime. Thus, from a Lagrangian perspective, one would expect ten dynamical degrees of freedom per point in spacetime, where each degree of freedom is specified by a pair of values – a generalized coordinate and its conjugate momenta (here, for example, a metric element and its first time derivative). However, four of the field equations do not contain second time derivatives of the metric, and therefore serve as *constraints*, eliminating four dynamical degrees of freedom (these four equations are usually called the *constraint equations*, and the six remaining equations the *evolution equations*). Furthermore, the geometry of spacetime is invariant under arbitrary coordinate transformations of the 4 spacetime coordinates, and choosing a particular coordinate system (or “gauge”) amounts to imposing four additional constraints, leaving only two dynamical degrees of freedom per spacetime point.

The presence of constraints and coordinate freedom in the Einstein equations permits considerable leeway in the solution method. One of the more common methods used these days is the so-called *free evolution* within the ADM (Arnowitt–Deser–Misner [28]) decomposition (see [29] for a thorough discussion of the various possibilities and corresponding classification scheme). Here, the 4 dimensional spacetime metric is written as a three dimensional spatial metric (six independent components), *lapse function* and a spatial *shift vector* (three components).² A coordinate system is chosen by specifying the lapse and shift, the constraint equations are solved at the initial time, and the spatial metric is then evolved in time using the evolution equations. In the continuum limit, the Bianchi identities (see [27], for example) guarantee that such an evolution scheme will preserve the constraints for all time, given appropriate boundary conditions.

The constraint equations are elliptic in nature, whereas the evolution equations are hyperbolic. Coordinate conditions can be chosen that give algebraic, elliptic, parabolic or hyperbolic equations for the kinematical variables (lapse and shift). Thus, even though it is always possible in principle to adopt a free evolution approach in the numerical solution of Einstein’s equations where elliptic equations are only solved at the initial time, there are nonetheless two situations where it may be preferable or necessary to solve one or more elliptic equations at each time step of the evolution. First, as just mentioned, it may be useful to adopt elliptic coordinate conditions. For example the choice of *maximal slicing* yields an elliptic equation for the lapse function, and the *minimal distortion* condition gives a set of elliptic equations for the shift vector components [39].

Second, in a numerical evolution, since the Bianchi identities will only be satisfied to within truncation error, the constraints can only be preserved to within truncation error [30]. This is not necessarily problematic, as the violation of the constraints should converge away in any consistent, stable numerical code. However, studies have indicated that with some formulations of the field equations, and using free evolution, certain constraint-violating modes grow exponentially with time, requiring prohibitively high accuracy (hence resolution) of the initial data and subsequent evolution to obtain a solution that is sufficiently close to the continuum one for the desired length of time integration [33,34,1]. One possible method to circumvent this problem is to use *constrained evolution* rather than free evolution; in this case one uses some number, m , $m \leq 4$, of the

¹ The notation 1D refers to problems with dependence on 1 spatial dimension, in addition to the implicit dependence on time; similarly for 2D and 3D.

² We emphasize that our counting is of second-order-in-space-and-time equations. A common approach is to recast the six second-order equations into a system of first-order equations, which result in additional auxiliary quantities that must be evolved, and additional constraints among the new quantities.

constraint equations to fix m of the dynamical variables, in lieu of the m second-order in time equations that would otherwise be used to update those quantities.³ Again, the expectation is that a stable numerical code will, in the continuum limit, provide a solution that is consistent with *all* of the field equations, including, in this case, those evolution equations that are not explicitly used in the overall update scheme. (Additionally, one hopes that violations in the evolution equations will not grow exponentially in time). To date, a significant majority of numerical codes use free evolution [1], and with the exception of [38] all constrained evolution simulations have been carried out in 1D or 2D.⁴

At this point, it is worth noting that there apparently is still an impression in the relativity community as a whole that elliptic equations are computationally expensive, and are thus to be avoided in numerical evolution if at all possible. However, provided that appropriate algorithms – such as the multigrid method – are adopted, this view is not consistent with at least some experience (see also [40] for fast elliptic solvers using spectral methods). In particular, as we will show below, the solution of the elliptic equations in our adaptive code requires roughly twice the CPU time required to solve the hyperbolic equations; furthermore, the solution cost of the elliptics scale *linearly* with the size of the computational domain. Thus, if one considers that in a free evolution an equivalent number of hyperbolic equations would need to be solved in lieu of the elliptic equations, the difference in cost is *not* a significant issue in deciding whether to tackle a particular problem using constrained versus free evolution.

We are thus lead to consider AMR algorithms for mixed elliptic/hyperbolic type, where our use of the term “hyperbolic” does not denote any formal definition of hyperbolicity, but instead is used to refer to an equation that is characterized by locality of influence. Now, a very well known AMR algorithm for hyperbolic equations is due to Berger and Olinger (B&O) [42]. This algorithm has several important properties that make it quite useful and efficient in solving certain classes of problems. These properties include dynamical regridding via local truncation error (TE) estimates, a grid-hierarchy composed of unigrid (single mesh) building blocks, and a recursive time-stepping algorithm that provides “optimal” efficiency in solving discretized evolution equations that are subject to a CFL-type stability condition. However, this algorithm, implemented verbatim for a mixed elliptic/hyperbolic system *cannot* be expected to work in general, due in part to the non-local nature of elliptic equations, and in part to the non-linear nature of the elliptic equations that tend to arise in numerical relativity. The reasons for this are as follows (a more detailed discussion is given in Section 3 and 4). In the B&O time-stepping procedure, a single, large time step is taken on a coarser level before several smaller time steps are taken on the interior, fine level. This is done so that the solution obtained on the coarse level can be used to set boundary conditions (via interpolation in time) for the subsequent fine level evolution. As the hierarchy is generated via local truncation error estimates, the solution obtained on the coarse level in the vicinity of the fine level boundaries will presumably be sufficiently accurate to allow one to use the coarse level solution to set fine level boundary conditions without adversely affecting the global solution. If the equations are hyperbolic, then a poorly resolved solution in the interior region of the coarse level will not have time to “pollute” the coarse/fine boundary region in only a single coarse level evolution step (and the coarse level solution is refreshed every time step with the fine level solution in the injection phase of the algorithm). This last statement is not true for elliptic equations in general, for then poorly resolved source functions in the interior of the coarse level could globally affect the accuracy of the solution obtained during the coarse level evolution step. For certain kinds of linear elliptic equations, such as the Poisson equation in Newtonian gravity, or that arising in the incompressible Navier–Stokes equations, one can circumvent this problem by taking advantage of conservation laws satisfied by source fields that couple to the elliptic equations (for example, with the Poisson equation in Newtonian gravity one can use a fine to coarse level injection function that preserves the matter energy density, and see for example [31] for a method for solving the Navier–Stokes equations with B&O style time sub-cycling). In general relativity the equations are non-linear, and furthermore

³ An alternative approach that has recently begun to receive some attention is *constraint-projection* (also called *chopped evolution* in [29]), where periodically during a free evolution the constraints are re-solved using a subset of the evolved solution supplied as free data for the constraint solve, and afterward the evolution is continued with this new “initial data” [35–37].

⁴ We should also mention here that there are alternative methods for evolving the field equation other than those based on a $3+1$ decomposition (see [1]); in particular, characteristic or null evolution has proven useful in many situations, and recently an AMR scheme for characteristic evolution has been proposed [41].

are coupled in such a manner that it is impossible to isolate such source functions in general. Therefore, to use B&O AMR in a constrained evolution, in particular its time-stepping algorithm, requires some modifications to deal with the elliptic equations; these modifications are the prime focus of this paper.

In Section 2, we first review the axisymmetric gravitational collapse code introduced in [32] that was used to develop the AMR approach described in this paper. This code solves a discretized version of the Einstein–Klein Gordon system of equations. We then review the original Berger and Oligier algorithm in Section 3, and then proceed to a description of the modifications we have made to handle elliptic equations in Section 4. Our primary modification involves a split of the solution of the elliptic equations into two phases. During the first phase, when hyperbolic equations are solved, functions satisfying elliptic equations are extrapolated to the advanced time level. The second phase is delayed until all finer levels have been evolved in the same fashion via recursion, and hence all levels at the same or finer resolution as the given one are in sync (i.e., have been evolved to the same physical time). Then, the elliptic equations are solved over the *entire* sub-hierarchy from the given level to the finest, using *extrapolated* boundary conditions from the parent (coarser) level at interior coarse-grid boundaries. In Section 5 we present several simulation results, including convergence tests and comparison with unigrid simulations. Concluding remarks are given in Section 6. All equations and finite-difference operators are listed in Appendix A, and some additional details of the AMR algorithm are given in Appendix B.

2. An axisymmetric gravitational collapse code

In this section we briefly review the physical system we are modeling (general relativity with a scalar field matter source), the PDEs governing the model, and the unigrid numerical code that computes an approximate finite-difference solution of the PDEs; additional details can be found in [32,43].

2.1. Equations, coordinate system and variables

The Einstein field equations can be written as

$$R_{\mu\nu} - \frac{1}{2}Rg_{\mu\nu} = 8\pi T_{\mu\nu}, \tag{1}$$

where $R_{\mu\nu}$ is the Ricci tensor, $R \equiv R^\mu_\mu$ is the Ricci scalar (using the Einstein summation convention where repeated indices are summed over), and we use geometric units where Newton’s constant, G , and the speed of light, c , are set to 1 [27]. With a massless scalar field Φ as the matter source, the stress-energy tensor $T_{\mu\nu}$ is given by

$$T_{\mu\nu} = 2\Phi_{;\mu}\Phi_{;\nu} - g_{\mu\nu}\Phi_{;\gamma}\Phi^{;\gamma}, \tag{2}$$

and the evolution of Φ is governed by the wave equation

$$\square\Phi \equiv \Phi^{;\mu}_{;\mu} = 0. \tag{3}$$

In these expressions a comma (,) is used to denote a partial derivative, and a semicolon (;) a covariant derivative.

Restricting attention to axisymmetric spacetimes without angular momentum, and choosing cylindrical coordinates, (t, ρ, z, ϕ) , adapted to the symmetry, we can write the spacetime metric as

$$ds^2 = -\alpha^2 dt^2 + \psi^4 [(d\rho + \beta^\rho dt)^2 + (dz + \beta^z dt)^2 + \rho^2 e^{2\bar{\sigma}} d\phi^2]. \tag{4}$$

The axial Killing vector is $(\partial/\partial\phi)^\mu$ and hence all the metric functions α , β^ρ , β^z , ψ and $\bar{\sigma}$, and the scalar field Φ depend only on ρ , z and t . Almost all coordinate freedom has been eliminated by choosing this form for the metric. What remains to be specified is a time-slicing, and for this we use maximal slicing, defined by

$$K = 0, \quad \frac{\partial K}{\partial t} = 0, \tag{5}$$

where $K \equiv K_a^a$ is the trace of the extrinsic curvature tensor K_a^b of $t = \text{const.}$ slices [39]. This gives an elliptic equation for α (A.2). The constraint equation subset of (1) gives three additional elliptic equations: the *Hamiltonian constraint*, which is viewed as an equation for ψ (A.3), and the ρ and z components of the *momentum constraint*, which are treated as equations for β^ρ (A.4) and β^z (A.5), respectively. One member of the evolution subset of (1) yields a second-order evolution equation for $\bar{\sigma}$, and the wave equation (3) provides a second-order hyperbolic equation for Φ . We convert both of these evolution equations to first-order-in time-form (A.7) and (A.9) by defining conjugate variables $\bar{\Omega}$ (geometry) and Π (matter) as follows:

$$\alpha \bar{\Omega} = -\bar{\sigma}_{,t} + 2\beta^\rho (\rho \bar{\sigma})_{,\rho^2} + \beta^z \bar{\sigma}_{,z} - \left[\frac{\beta^\rho}{\rho} \right]_{,\rho}, \quad (6)$$

$$\Pi \equiv \frac{\psi^2}{\alpha} (\Phi_{,t} - \beta^\rho \Phi_{,\rho} + \beta^z \Phi_{,z}). \quad (7)$$

Thus we end up with a system of eight equations for eight variables – α , ψ , β^ρ and β^z satisfy elliptic equations, and $\bar{\sigma}$, $\bar{\Omega}$, Φ and Π satisfy hyperbolic equations.

2.2. Boundary conditions

On the axis at $\rho = 0$, the following regularity conditions must be enforced in order that spacetime remain locally flat in the vicinity of the axis:

$$\begin{aligned} \alpha_{,\rho} &= 0, \\ \psi_{,\rho} &= 0, \\ \beta^z_{,\rho} &= 0, \\ \beta^\rho &= 0, \\ \bar{\sigma} &= 0, \\ \bar{\Omega} &= 0, \\ \Phi_{,\rho} &= 0, \\ \Pi_{,\rho} &= 0. \end{aligned} \quad (8)$$

At the outer boundaries $\rho = \rho_{\text{max}}$, $z = z_{\text{max}}$ and $z = z_{\text{min}}$, for the hyperbolic variables approximate outgoing radiation (Sommerfeld) conditions are imposed,⁵ while for the elliptic equations, conditions based on asymptotic flatness conditions are used

$$\begin{aligned} \alpha &= 1, \\ \psi - 1 + \rho \psi_{,\rho} + z \psi_{,z} &= 0, \\ \beta^z &= 0, \\ \beta^\rho &= 0, \\ r \bar{\sigma}_{,t} + \rho \bar{\sigma}_{,\rho} + z \bar{\sigma}_{,z} + \bar{\sigma} &= 0, \\ r \bar{\Omega}_{,t} + \rho \bar{\Omega}_{,\rho} + z \bar{\Omega}_{,z} + \bar{\Omega} &= 0, \\ r \Phi_{,t} + \rho \Phi_{,\rho} + z \Phi_{,z} + \Phi &= 0, \\ r \Pi_{,t} + \rho \Pi_{,\rho} + z \Pi_{,z} + \Pi &= 0. \end{aligned} \quad (9)$$

⁵ These conditions assume that spacetime is nearly flat at the outer boundary, and that disturbances (radiation) in both the scalar and gravitational fields are propagating purely radially, and have $1/r$ falloff.

```

As an initial guess to the solution at time  $t_1$ , copy variables
from  $t_0$  to  $t_1$ ;

repeat
  perform 1 Newton–Gauss–Seidel relaxation sweep of the
    evolution equations, solving for the unknowns at time  $t_1$ ;
  perform 1 multigrid vcycle on the set of elliptic equations,
    discretized at time  $t_1$ ;
until (residual norm < tolerance)

```

Fig. 1. A pseudo-code description of the iteration we use to solve the system of coupled hyperbolic/elliptic equations on a single mesh.

2.3. Unigrid numerical scheme

The set of eight PDEs are solved using second-order accurate finite difference (FD) techniques. The elliptic equations are solved using an FAS (full approximation storage) multigrid algorithm with V-cycling [46,47]. At $t = 0$, $\bar{\sigma}$, $\bar{\Omega}$, Φ and Π are freely specified, after which the remaining variables α , β^p , β^z and ψ are obtained by solving the corresponding elliptic equations. To evolve the variables with time, the hyperbolic equations are discretized using an iterative Crank–Nicholson scheme, with Kreiss–Oliger [44] dissipation added to reduce unwanted (and un-physical) high-frequency solution components (“noise”) of the FD equations. This iteration involves variables at two time levels: the known solution at $t = t_0$, and the unknowns, solved for using Newton–Gauss–Seidel relaxation implemented in RNPL [45], at $t = t_1 = t_0 + \Delta t$. After each iteration, the elliptic variables are updated at $t = t_1$ by applying a single V-cycle. This process is repeated until the infinity norm of the residual of all equations is below some specified tolerance. The pseudo-code in Fig. 1 summarizes this iteration sequence.

Specific difference operators used to discretize the equations are summarized in Appendix A.3.

3. The Berger and Oliger AMR algorithm

Here we briefly review some aspects of the B&O AMR algorithm for hyperbolic PDEs that are of relevance to this paper, in particular the grid hierarchy and time-stepping procedure.

3.1. AMR grid hierarchy

In the Berger and Oliger AMR algorithm, the computational domain is decomposed into a hierarchy of uniform meshes (see Fig. 2) with the following properties:

- The hierarchy contains ℓ_f levels. Each level ℓ contains grids of the same resolution – the coarsest grids are in level 1 (the *base grid*), the next-coarsest in level 2, and so on until level ℓ_f , which contains the finest grids in the hierarchy.
- The ratio of discretization scales $h_\ell/h_{\ell+1}$ between levels ℓ and $\ell + 1$ is called the *spatial refinement ratio* $\rho_{s,\ell}$. $\rho_{s,\ell}$ is typically an integer greater than or equal to 2. For simplicity, we will also assume that $\rho_{s,\ell}$ is the same for all levels, and therefore use the symbol ρ_s to denote the spatial refinement ratio.
- All grids at level $\ell + 1$ (*child grids*) are *entirely* contained within grids at level ℓ (*parent grids*). Grids at the same level may overlap.
- In the simplified variant of the B&O algorithm described here, we require that all grids within the hierarchy share the same coordinate system. In particular, this implies that all grid boundaries run parallel to the corresponding boundaries of the computational domain. In addition, a child grid must be aligned relative to its parent grid such that all points on the parent grid, within the common overlap region, are coincident with a point on the child level. The original B&O algorithm allowed for a child grid to be rotated relative to its parent.

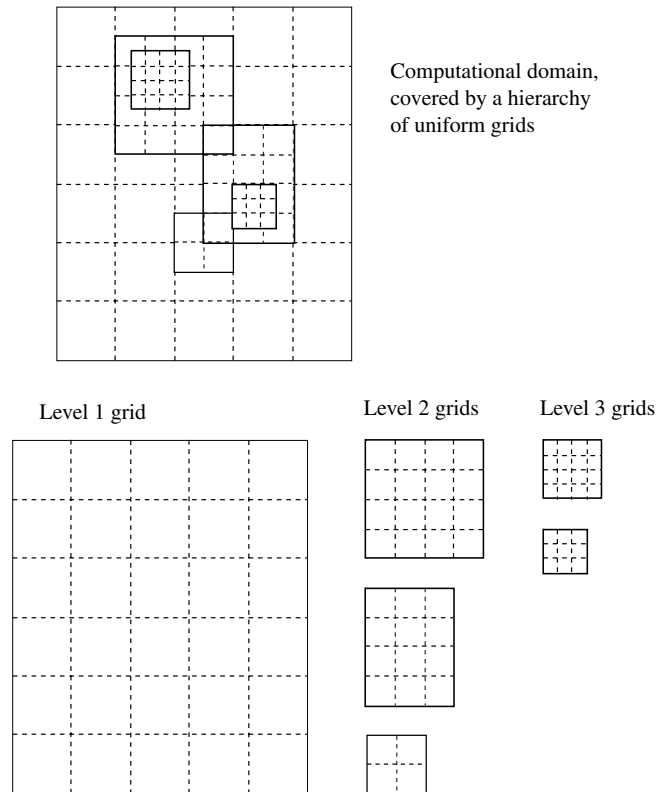


Fig. 2. An example of a Berger and Olinger mesh hierarchy. The hierarchy consists of a number of *levels*, where each level contains a set of uniform meshes of the same spatial resolution. Our convention is to let higher level numbers denote levels consisting of grids with higher resolution (smaller mesh spacing, h), beginning with level 1 for the coarsest mesh. The upper diagram shows the computational domain, covered by a three-level-deep hierarchy. The plots below this demonstrate how the hierarchy is stored in memory, namely as a collection of individual grids. Thus a given point, \vec{x} in the computational domain can be contained/represented in multiple grids in the Berger and Olinger scheme.

The particular grid structure that exists at any given time is calculated by computing local truncation error estimates, so that at any point $\vec{x} \equiv (\rho, z)$ within the computational domain the finest grid covering that point has sufficient resolution to adequately resolve all features of the solution there. This is an important property of the grid hierarchy, not only for the obvious reason of providing the desired resolution everywhere, but it justifies the use of the B&O time-stepping algorithm to evolve the hierarchy, as we now review.

3.2. The Berger and Olinger time-stepping algorithm

The B&O recursive time-stepping algorithm was designed to solve hyperbolic equations, discretized on the AMR grid hierarchy. The basic ideas behind this update scheme are as follows. The hierarchy is evolved in time through a particular sequence of unigrid time-steps, performed on individual grids within the hierarchy. A time step of size Δt_ℓ is taken on all grids at level ℓ , before a number $\rho_{t,\ell}$ (the *temporal refinement ratio*) time steps of size $\Delta t_{\ell+1} = \Delta t_\ell / \rho_{t,\ell}$ are taken on level $\ell + 1$. The preceding rule is applied recursively, from the coarsest to finest level in the hierarchy. In general, $\rho_{t,\ell}$ must be an integer greater than or equal to $\rho_{s,\ell}$ in order to satisfy the CFL condition on all levels in the hierarchy if it is satisfied on the coarsest level. As with ρ_s , we only consider a constant temporal refinement ratio ρ_t for all levels. The reason why a time step is first taken on coarse level ℓ is that the solution obtained there at time $t + \Delta t_\ell$ is then used to set boundary conditions, via interpolation in time, for the subsequent time steps on the finer level $\ell + 1$ (unless some portion of the fine level abuts the boundary of the computational domain, in which case the physical/mathematical boundary

```

repeat  $N$  times: call single_step(1);
stop;

subroutine single_step(level  $\ell$ )
  if (regridding time for level  $\ell$ ) then
    regrid from levels  $\ell$  to  $\ell_f$ ;
  end if

  if ( $\ell > 1$ ) then
    set boundary conditions along AMR boundaries at time
       $t_\ell + \Delta t_\ell$  via interpolation from level ( $\ell - 1$ );
  end if

  perform 1 evolution step on all grids at level  $\ell$ ;

   $t_\ell := t_\ell + \Delta t_\ell$ ;

  if ( $\ell < \ell_f$ ) then
    repeat [ $\rho_t := \Delta t_\ell / \Delta t_{\ell+1}$ ] times: call single_step( $\ell + 1$ );
    inject the solution from level  $\ell + 1$  to level  $\ell$ 
      in the region of overlap between levels  $\ell$  and  $\ell + 1$ ;
  end if

end of subroutine single_step

```

Fig. 3. A pseudo-code representation of the Berger and Olinger time stepping algorithm.

conditions of the original problem can be applied.) It is possible to do this because the solution obtained on the coarse level in the vicinity of the finer level boundary will be *as accurate*, to within the specified truncation error, as a putative solution would have been that was obtained on a fine level encompassing the entire computational domain.⁶ The solution obtained on the coarse level interior to this boundary will not be as accurate; however, the assumed hyperbolic nature of the PDEs will protect this inaccuracy from polluting the coarse/fine boundary region within a single coarse level time step.

After ρ_t time-steps on level $\ell + 1$, when the solution on grids at levels ℓ and $\ell + 1$ are again in synchrony, grid functions from level $\ell + 1$ are *injected* into the coarse grids at level ℓ , in the region of overlap between the two levels. Thus, the most accurate solution available at a given point \vec{x} is continuously propagated to all grids in the hierarchy that contain \vec{x} . Injection simply consists of copying values from level $\ell + 1$ to level ℓ at common points (in the more general B&O algorithm, where finer levels can be rotated relative to coarser levels, the injection step requires some form of interpolation). Fig. 3 is a pseudo code description of the B&O time-stepping procedure just described.

4. Berger and Olinger style AMR for constrained evolution

The locality argument given in the preceding section to justify the use of the B&O evolution algorithm is only applicable to hyperbolic equations, for then the finite speed of propagation prevents contamination of the solution in the boundary region of a coarse level by a poorly resolved solution in the interior. Solutions to elliptic equations do not share this property, and therefore it is not feasible to solve for such equations on the coarse grid alone, with the intention of supplying boundary conditions for subsequent fine grid time steps.⁷ One way to circumvent this problem is to abandon the B&O recursive time-stepping procedure. In other words, one could evolve the entire hierarchy forward in time with a global time step, for example by perform-

⁶ Assuming that the specified maximum TE estimate used in the construction of the grid hierarchy is sufficiently small that the solution is within the convergent regime, and hence the TE estimate is a good approximation to the actual solution error.

⁷ Except, as mentioned in Section 1, for certain kinds of linear systems, where the source terms appearing in the elliptic equations can cleanly be identified and coarsened in a manner that conserves the source “energy density”. This is not possible for the Einstein equations, which are fundamentally non-linear, since the gravitational field acts as its own source.

ing a Crank–Nicholson style iteration as in the unigrid code (see Section 2.3). A major drawback to this method is that, to satisfy the CFL condition, the global time step will need to be set to $\lambda\Delta\rho(\ell_f)$, where $\Delta\rho(\ell_f)$ is the cell size on the *finest* level ℓ_f in the hierarchy, and $0 < \lambda \lesssim 1$ is a constant. This would require that one take $\rho_t^{\ell_f-\ell} - 1$ additional time steps at level ℓ for each time step that the usual B&O algorithm would have taken.

The technique that we propose here to incorporate elliptic equations into the standard B&O time-stepping framework is to employ a combination of *extrapolation and delayed solution* of the elliptic variables (see Fig. 4). Simply stated, on coarse levels one does *not* solve the elliptic equations during the evolution step of

```

repeat  $N$  times: call single_step(1);
stop;

subroutine single_step(level  $\ell$ )
  if (regridding time for level  $\ell$ ) then
    regrid from levels  $\ell$  to  $\ell_f$ ;
  end if

  for hyperbolic variables: if ( $\ell > 1$ ) then set boundary conditions along
    AMR boundaries at time ( $t_\ell + \Delta t_\ell$ ) via interpolation from level  $\ell - 1$ ;

  for elliptic variables: extrapolate the entire grid function to time
    ( $t_\ell + \Delta t_\ell$ ) from earlier-time values;

  repeat
    if ( $\ell = \ell_f$ ) then perform 1 multigrid vcycle on elliptic variables
      at time ( $t_\ell + \Delta t_\ell$ );
    perform 1 iteration of the Crank–Nicholson sweep for all
      hyperbolic variables;
  until (residual norm < tolerance)

   $t_\ell := t_\ell + \Delta t_\ell$ ;

  if ( $\ell < \ell_f$ ) then
    repeat [ $\rho_t := \Delta t_\ell / \Delta t_{\ell+1}$ ] times: call single_step( $\ell + 1$ );
    compute the truncation error estimate for level  $\ell + 1$  by subtracting
      the solution in the region of overlap between levels  $\ell$  and  $\ell + 1$ ;
    inject the solution from level  $\ell + 1$  to level  $\ell$ 
      in the region of overlap between levels  $\ell$  and  $\ell + 1$ ;
  end if

  if ( $\ell = 1$  or ( $\ell < \ell_f$  and  $t_\ell \neq t_{\ell-1}$ )) then
     $t := t_\ell$ ;
    do  $\ell_0 := \ell + 1$  to  $\ell_f$ 
      for each elliptic variable  $f_{\ell_0}(t)$  :  $\hat{f}_{\ell_0}(t) := f_{\ell_0}(t)$ ;
    end do
    re-solve the elliptic equations over the sub-hierarchy [ $\ell.. \ell_f$ ] at time  $t$ ;
    do  $\ell_0 := \ell + 1$  to  $\ell_f$ 
      for each elliptic variable  $f_{\ell_0}(t)$  :
         $\Delta f_{\ell_0}(t) := f_{\ell_0}(t) - \hat{f}_{\ell_0}(t)$ ;
         $f_{c\ell_0}(t) := \Delta f_{\ell_0}(t) / \rho_t^{\ell_0-\ell}$ ;
         $f_{\ell_0}(t - \rho_t \Delta t_{\ell_0}) := f_{\ell_0}(t - \rho_t \Delta t_{\ell_0}) + \Delta f_{\ell_0}(t) - f_{c\ell_0}(t)$ ;
      end do
    end if

  end of subroutine single_step

```

Fig. 4. A pseudo-code representation of the modified Berger and Olinger time stepping algorithm described in Section 4; compare to the original algorithm in Fig. 3. Notice that here we have expanded the “perform 1 evolution step...” statement in Fig. 3 to highlight the fact that in the modified algorithm the finest level is treated differently than the coarser levels then (though the *particular* details of the evolution step are not significant – for concreteness we list the same scheme as used in the unigrid code). Here we also show where the truncation error estimate is computed when using a self-shadow hierarchy (see Appendix B).

the algorithm; rather, one extrapolates the corresponding variables to the advanced time from the solution obtained at earlier times. The solution of the elliptic equations is delayed until *after* the injection of fine grid (level $\ell + 1$) values into the parental coarse grids (level ℓ). At that stage, all levels from ℓ to ℓ_f are in sync, and the elliptic equations are solved over the *entire resulting subset* of the hierarchy, with boundary conditions on AMR boundaries of level ℓ set via extrapolation. This ensures that all details from finer grids interior to level ℓ are represented in the solution.

One of the non-trivial aspects of this technique is the method used to extrapolate the elliptic variables, which we now describe. We use linear (second order) extrapolation in time, with periodic *corrections* to try to account for changes that occur upon global multigrid solves. For level ℓ , $\ell > 1$, the two past-times used in the extrapolation are the two most recent times *when levels ℓ and $\ell - 1$ were in sync* (thus, at times when a solution of the elliptic variables involving at least levels $\ell - 1$ to ℓ_f was obtained); in other words, every ρ_t steps we save the elliptic variables for use in extrapolation⁸ (see Appendix B.5 for a pseudo-code description of how the past time levels are initialized for the very first time step of evolution). For level $\ell = 1$, the two most recent time levels are used for extrapolation.⁹ The correction, applied only to levels $\ell > 1$, is calculated as follows. Whenever level ℓ is in sync with level $\ell_c, \ell_c + 1, \dots, \ell_f + 1, \ell_f$, where $\ell_c < \ell$, a multigrid solve takes place over levels ℓ_c, \dots, ℓ_f . Denote by $\hat{f}_\ell(t)$ the value of a variable f at level ℓ , calculated via extrapolation from $f(t - \rho_t \Delta t_\ell)_\ell$ and $f(t - 2\rho_t \Delta t_\ell)_\ell$, and let $f_\ell(t)$ denote the value of the same variable *after* the multigrid solve at time t (note that for simplicity in notation we have dropped the spatial coordinate dependence of the variable f). As illustrated in Fig. 5, the correction contains two components:

$$\Delta f_\ell(t) \equiv f_\ell(t) - \hat{f}_\ell(t) \text{ and } f_{c\ell}(t) \equiv \frac{\Delta f_\ell(t)}{\rho_t^{\ell - \ell_c}}, \tag{10}$$

which are used to change the *past* time value $f_\ell(t - \rho_t \Delta t_\ell)$ as follows:

$$f_\ell(t - \rho_t \Delta t_\ell) \rightarrow f_\ell(t - \rho_t \Delta t_\ell) + \Delta f_\ell(t) - f_{c\ell}(t) \tag{11}$$

The logic behind this form of correction stems from a couple of observations about how the re-solved solution differs from the extrapolated solution, and how some adaptive solutions differ from unigrid solutions of comparable resolution. First, in general $\Delta f_\ell(t)$ is (in a loose sense) proportional to $\ell_c - \ell$; i.e., the more levels over which the elliptic equations are re-solved, the larger the change in the interior, finer level ℓ solution. However, the change in the interior part of the solution induced by the global solve tends to be a near constant shift, leaving finer details of the interior solution unchanged. Second, the local “velocity” $f_\ell(t) - f(t - \rho_t \Delta t_\ell)_\ell$ (calculated *prior* to the correction) tends to be represented quite accurately in the adaptive solution scheme. Therefore the $\Delta f_\ell(t)$ part of the correction preserves this velocity for subsequent extrapolation, and is in fact essential for the stability of the algorithm with a deep hierarchy, as then the global shift is often larger in magnitude than the local velocity. The second part of the correction $f_{c\ell}(t)$ is an attempt to improve the accuracy of the extrapolation, for if in hindsight the quantity $f_{c\ell}(t)$ had been added to f at each one of the $\rho_t^{\ell - \ell_c}$ intermediate time steps between solves over levels ℓ_c, \dots, ℓ_f , then $\Delta f_\ell(t)$ would be zero at time t (ignoring, of course, the effect that this putative correction would have had on the solution).

One last comment regarding the extrapolation: on the finest level of the hierarchy, the elliptic equations are solved via the usual interleaved Crank–Nicholson/V-cycle iteration as discussed in Section 2.3; then the extrapolation simply serves to set boundary conditions.

5. Results

The extrapolation technique described in the previous section is rather ad hoc, though both the choice of which past times to extrapolate from and the use of corrections play a significant role in the stability and accu-

⁸ Early experiments using the values from the two most recent time steps of level ℓ for extrapolation resulted in unstable evolution.

⁹ Though note that in our algorithm level 1 is *always* fully refined because of the self-shadow hierarchy mechanism we use for truncation error estimation (see Appendix B.1), and therefore level 2 should be considered the “true” coarsest level of the hierarchy (in effect, level 1 is only used for truncation error estimation).

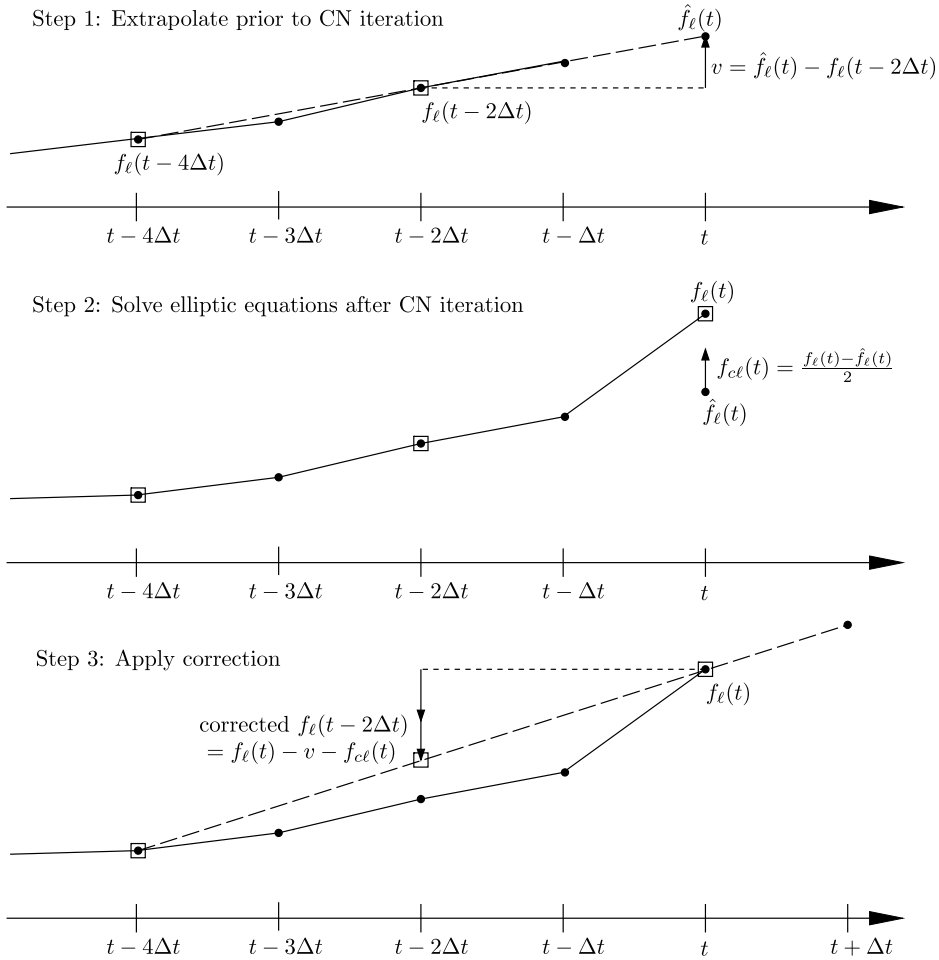


Fig. 5. An illustration of the technique used to extrapolate and solve for elliptic variables within the AMR framework. In this example, we show the evolution of an elliptic variable f_ℓ from $t - \Delta t$ to t , assuming that $\rho_i = 2$ and $\ell < \ell_f$. Initially (step 1), f_ℓ at t is calculated via linear extrapolation from data at past times $t - 2\Delta t$ and $t - 4\Delta t$ (quantities used for extrapolation are depicted by boxes in the diagram). This value, labeled $\hat{f}_\ell(t)$, is used during the solution of the hyperbolic variables (via Crank–Nicholson iteration (CN) here). At time t , we assume levels ℓ and $\ell_c = \ell - 1$ are in sync, and so after the CN iteration (and *after* the equations on finer levels $\ell + 1 \dots \ell_f$ have been evolved to t) the elliptic equations are re-solved over levels $\ell_c \dots \ell_f$ (step 2). This results in a change in the value of f from $\hat{f}_\ell(t)$ to $f_\ell(t)$ (for simplicity we assume that a similar change that occurred at time $t - 2\Delta t$ is zero). This change is propagated back to $t - 2\Delta t$, so that the same velocity v , *modulo a correction* $f_{c\ell}(t)$, will be used to extrapolate f to $t + \Delta t$ (step 3). Here, since $\ell - \ell_c = 1$, the correction is such that one is effectively extrapolating from $t - 4\Delta t$ and t to time $t + \Delta t$; this would not be the case otherwise – see (10,11). (If $\ell = \ell_f$, then the elliptic variables are solved within the CN iteration, and the value obtained afterward is used for $\hat{f}_\ell(t)$.)

racy of the adaptive evolution code. In this section we present some results showing the effectiveness of the algorithm.

5.1. Comparison with a unigrid evolution

The first test of the algorithm presented here is a comparison of unigrid evolutions to a similar AMR evolution (test results on the convergence properties of the unigrid code can be found in [32]). Specifically, we compare an evolution obtained with the AMR code to a unigrid evolution, where the entire unigrid mesh is given the resolution h of the finest level in the AMR hierarchy. To gauge how well the AMR solution approximates the unigrid one, we then compare the unigrid solution to that obtained with two additional unigrid runs, with resolutions of $2h$ and $4h$. In certain respects this is not a very stringent test, as limited

computational resources do not allow us to run using very high resolution unigrid simulations (which of course is the motivation for pursuing AMR). Also, the accuracy of the AMR solution will largely depend on the structure of the grid hierarchy, which is (predominantly) controlled by the maximum allowed TE. Thus, in principle one could obtain better agreement between the AMR and unigrid simulations by decreasing the TE parameter while keeping the maximum depth of the AMR hierarchy fixed. Nevertheless, this comparison *does* demonstrate that the adaptive algorithm works in practice.

The initial data for this example is a time symmetric scalar field pulse:

$$\Phi(0, \rho, z) = A \exp \left[-\frac{\rho^2 + z^2}{\Delta^2} \right], \tag{12}$$

with $A = 0.23$ and $\Delta = 1.0$ (all other free fields are set to 0 at $t = 0$). This amplitude is sufficiently large that the solution is in the non-linear regime (and thus close to forming a black hole). The outer boundary is at $\rho_{\max} = z_{\max} = -z_{\min} = 10$. The maximum value for the TE is set to 10^{-5} (only Φ and Π are used in the calculation of the TE – see [Appendix B](#)). The resolution of the base grid is 65×129 , with $\rho_s = 2$, and up to three additional levels of refinement. Thus, level 4 has an effective resolution of 513×1025 , and so we choose unigrid comparison runs with resolutions of 513×1025 (h), 257×513 ($2h$) and 129×257 ($4h$). The Courant factor is $\lambda = 0.3$ for all runs, and the physical time at the end of each simulation is $t \sim 2.8$ (which corresponds to 480 time steps on the level with the finest resolution).

[Fig. 6](#) shows a plot of the conformal factor ψ at $t = 2$ from the adaptive simulation, with grid bounding boxes overlaid to give an idea of the structure of the hierarchy adaptively generated by the AMR code. [Fig. 7](#) shows ℓ_2 norms of the differences between the solutions generated by the h resolution unigrid simulation and the two lower resolution unigrid and adaptive simulations. For brevity we only show differences for the four elliptic variables; differences in the hyperbolic variables exhibit similar behavior. What [Fig. 7](#) demonstrates is that, compared to the h unigrid simulation, the adaptive solution has accuracy comparable to the $2h$ simulation, and significantly greater accuracy than the $4h$ simulation, even though (as illustrated in [Fig. 6](#)) the majority of the coordinate domain in the adaptive solution is spanned by a grid with less resolution than either that of the $2h$ or $4h$ simulations. [Fig. 8](#) is a comparison of the time-difference of the maximum (or minimum, as appropriate) of the elliptic variables ψ , α , β^ρ and β^z from the h unigrid and adaptive simulations. The time-difference $\Delta f / \Delta t$ is calculated as $(f^{n+1} - f^n) / \Delta t$, where f^n denotes one of the quantities, ψ , α , β^ρ or β^z at time step n . [Fig. 8](#) demonstrates two interesting aspects of the extrapolation scheme of the adaptive code. First, the high frequency temporal “noise” that is apparent in the adaptive solution of the elliptic variables (and that has been exaggerated in the figure by taking a time-difference) does not adversely affect the accuracy of the solution on average. Second, the presence of such noise suggests why linear extrapolation at level ℓ from the most recent times of level ℓ is unstable; however, it is not so obvious why extrapolation from past times that are in-sync with a parent level ($\ell - 1$ or less) results in stable evolution. Note that with the particular system of equations solved for here (summarized in [Appendix A](#)) *no* explicit time derivatives of any elliptic

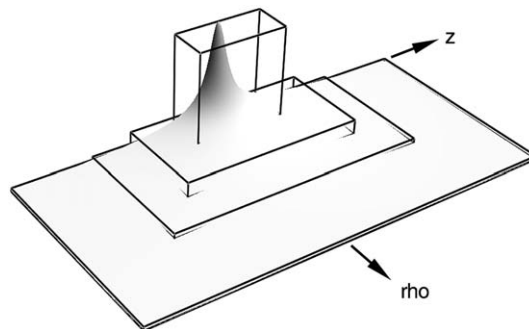


[Fig. 6](#). A surface plot of ψ at $t = 2$ from the adaptive simulation discussed in [Section 5.1](#), where the height of the surface is proportional to the magnitude of ψ (ranging approximately from 1 at the outer boundary to 1.5 at the origin $\rho = z = 0$). Overlaid on the surface are the AMR grid bounding boxes – the smallest, interior box has the finest resolution, corresponding to an effective unigrid resolution of 513×1025 .

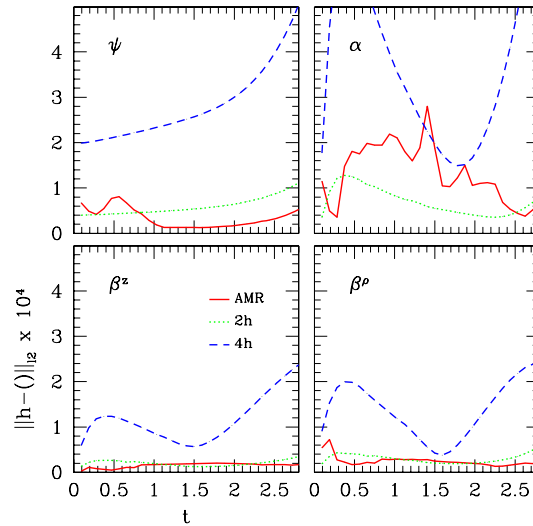


Fig. 7. Comparison between unigrid and adaptive simulation results for the elliptic variables ψ , α , β^p and β^z , as discussed in Section 5.1. Shown here are ℓ_2 norms of differences between the solution generated by the h resolution (513×1025) unigrid simulation and each of the solutions produced by two lower resolution unigrid simulations, $2h$ (257×513) and $4h$ (129×257), and an adaptive simulation (see Fig. 6 for a representative sample of the mesh structure from the AMR solution at $t = 2$, where the base level 1 has resolution 65×129 , and the finest level 4 has the same resolution as the h unigrid run). Thus, we are using the h unigrid solution as a benchmark, and the plots show that the adaptive solution is of comparable accuracy to the $2h$ unigrid solution, and of significantly greater accuracy than the $4h$ unigrid solution, despite that the majority of the coordinate domain of the AMR solution is covered by grids with mesh spacing h_i satisfying $h_i > 4h > 2h$.

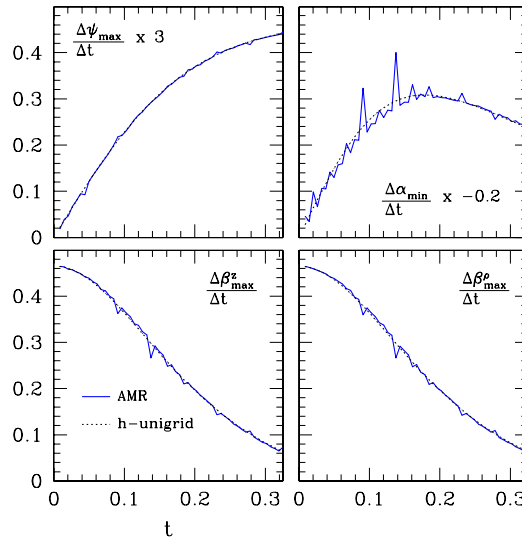


Fig. 8. Comparison between h resolution (513×1025) unigrid and adaptive simulations results as discussed in Section 5.1, showing the time-difference of the maximum (or minimum, as appropriate) of the elliptic variables ψ , α , β^p and β^z . For clarity, only about 50 time-steps are shown, and the differences for α and ψ have been scaled by constants to fit all the plots on the same vertical scale. The time-difference $\Delta f / \Delta t$ is calculated as $(f^{n+1} - f^n) / \Delta t$, where f^n labels one of the above quantities at time step n . These figures demonstrate a couple of interesting aspects of the extrapolation scheme for the adaptive code. First, the high frequency “noise” that is apparent in the adaptive solution (which has been exaggerated here by taking a time-difference) does not adversely affect the accuracy of the solution on average. Second, the presence of such noise suggests why linear extrapolation from the most recent time levels is unstable (though it is not obvious why extrapolation from past time levels that are in-sync with a parent level results in stable evolution).

quantities appear. Furthermore, during the evolution phase of the algorithm (see Section 2.3), the Crank–Nicholson differencing scheme only couples the time average (over two time steps) of elliptics variables to the hyperbolic equations, providing a certain amount of temporal smoothing. Thus, the results shown in

Table 1
Timing information for the tests described in Section 5.1

	Unigrid-4 <i>h</i>	Unigrid-2 <i>h</i>	Unigrid- <i>h</i>	AMR
Runtime (s)	4.45×10^2	4.48×10^3	3.31×10^4	2.19×10^3
Total number of grid points	4.01×10^6	3.18×10^7	2.54×10^8	1.97×10^7
Average time per grid point (μ s)	111	141	131	111

The *runtime* is the wall time taken (on a 2.4 GHz Intel XEON processor), in seconds, for each simulation, including initial data calculation and evolution. The *total number of grid points* is a count of all the grid points, in space and time, at which a solution was obtained during the simulation. This includes the grid points used during calculation of the initial data, and the calculation of the initial hierarchy for the adaptive run. The *average time per grid point* (in microseconds) is the runtime divided by the total number of grid points. What these numbers suggest (see also Table 2) is that the computational cost of this solution method scales approximately linearly with the total number of grid points, and that the computational overhead for the adaptive algorithm is negligible. Note however that we have *not* taken into account that in the adaptive hierarchy certain coordinate locations are covered by multiple points, and therefore there is some “wastage” in the AMR calculation. In this particular simulation, at any one time between 15% and 20% of the points in the adaptive hierarchy were redundant, and this should be viewed as an additional (and unavoidable) overhead to the per-point cost of this Berger and Olinger style AMR algorithm.

Fig. 8 suggest that modifications to the extrapolation scheme may be needed for systems of PDEs that use other methods to difference in time, or if time derivatives of variables solved for using elliptic equations couple to the hyperbolic equations.

5.1.1. Timing information

We conclude this section by presenting timing information in Table 1 above for the comparison test just described. This serves to show that, at least for the elliptic-hyperbolic system considered here, the overhead of the AMR algorithm is negligible, and that the solution time scales roughly linearly with the total number of grid points in the discrete solution. See also Section 5.2.1, which contains more detailed information on the percentage of time spent in various stages of the algorithm for the test simulations presented in the next section.

5.2. Convergence and consistency tests

In this section we present some convergence test results, providing evidence that the overall AMR solution scheme *is* stable and convergent. We also compare the solution of the conformal factor ψ to that obtained in a *partially constrained* evolution, where α , β^{ρ} and β^z are solved as described in Section 2 via the slicing condition and momentum constraints respectively, but where a hyperbolic evolution equation (A.10) obtained from the maximal slicing condition $K = 0$, rather than the elliptic Hamiltonian constraint, is now used to update ψ .¹⁰ In the continuum limit, and the limit where the outer boundary position goes to infinity, the solution obtained from fully and partially constrained evolution should (assuming both numerical implementations are consistent and stable) converge to a unique solution of the Einstein equations. In the partially constrained evolution, ψ is evolved as a hyperbolic variable, and thus within the traditional B&O time stepping framework; however, during fully constrained evolution ψ is solved for using an elliptic equation using the new AMR technique. Thus, demonstrating convergence to a consistent solution for ψ is a rather non-trivial test of the modified AMR algorithm.

We use the following technique to calculate convergence factors for the adaptive code. We choose a “modest” value (10^{-3} in this case) for the maximum allowed TE (calculated as described in Appendix B.1), run a simulation, and save a copy of the dynamical grid structure produced during the evolution. The solution on this grid hierarchy will serve as the coarsest resolution simulation, labeled 4*h*. For the higher resolution simulations 2*h* and *h*, We rerun the code with identical initial data, and use the same grid hierarchy produced by the 4*h* case *except* that the resolution of all grids in the hierarchy is doubled (quadrupled) for the 2*h* (*h*) simulation; the Courant factor is kept constant, hence the number of time-steps taken per level also doubles

¹⁰ That an independent equation (other than the Hamiltonian constraint) exists for ψ is due to the over-determinism in the Einstein equations, as discussed in Section 1.

(quadruples). Then, by assuming the usual Richardson expansion, one can compute a convergence factor Q_f^h for a variable f via

$$Q_f^h \equiv \frac{\|f_{4h} - f_{2h}\|_2}{\|f_{2h} - f_h\|_2}, \quad (13)$$

where f_{4h} is the solution on the $4h$ hierarchy, and similarly for f_{2h} and f_h . In (13), the subtraction of grid functions is only defined at common points between the hierarchies (every other point of the finer mesh in this case). The ℓ_2 norm of a grid function f is taken point-wise as follows:

$$\|f\|_2 = \frac{\left(\sum_{\ell} \sum_g \sum_{i,j} f_{\ell}(\rho_g + i\Delta\rho_{\ell}, z_g + j\Delta z_{\ell})^2\right)^{1/2}}{\sum_{\ell} \sum_g \sum_{i,j} 1}, \quad (14)$$

where the sum over ℓ is the sum over all levels in the hierarchy where f is defined (so for the differences in (13) this will be all levels except the finest), the sum over g is over all grids at the given level, and the sum over (i, j) covers all points within a given grid, where (ρ_g, z_g) is the location of the $(i = 0, j = 0)$ point. Note that such a point-wise norm is biased (compared to an area-weighted norm, such as an integral norm) toward the highest resolution region of the domain, where most of the points are clustered. This is desirable for the solution presented here, where the region of high refinement is centered on a very small part of the domain, and outside of this region the solution is slowly varying and well represented by the coarse mesh. An area-weighted norm in this case would almost completely ignore information on the finest levels. For a “residual” function R , in other words a function that should converge to zero in the limit as $h \rightarrow 0$, we use the following expression for its convergence factor:

$$Q_R^h \equiv \frac{\|R_{2h}\|_2}{\|R_h\|_2}. \quad (15)$$

For a second-order accurate finite difference scheme one expects both Q_f^h and Q_R^h to approach 4 asymptotically.

The initial data for this example is also a time symmetric scalar field pulse given by (12), with $A = 0.25$ and $\Delta = 0.5$, and all other free fields set to 0 at $t = 0$. Adopting apparent horizon detection as our operative definition of black hole existence, in this case a black hole (with mass $M \sim 0.12$ in geometric units) *does* form by $t \sim 2.5$.

Computationally, relevant parameter settings are as follows. The outer boundary is at $\rho_{\max} = z_{\max} = -z_{\min} = 32$, and for the $4h$ simulation the resolution of the base grid is 65×129 . The maximum value for the TE is set to 10^{-3} ; this results in a grid hierarchy containing three additional levels ($\rho_s = 2:1$) at $t = 0$, and six additional levels at the end of the simulation.¹¹ See Fig. 9 for sample plots of ψ at $t = 0$ and $t = 3$ to illustrate the grid hierarchy. The effective finest grid resolution for the h simulation is roughly $16,000 \times 32,000$, making it impractical to do a unigrid comparison in this case. Fig. 10 shows the calculated convergence factors for the four elliptic quantities ψ , α , β^{ρ} and β^z , and Fig. 11 contains the convergence factor for $\psi_c - \psi_f$, where ψ_c is the conformal factor ψ from fully constrained evolution, and ψ_f is the conformal factor calculated from the free evolution of ψ . These plots show reasonable convergence and consistency results, with a couple of caveats discussed in the captions.

5.2.1. Timing information

Table 2 contains some timing information for the set of simulations described in this section. The major point we would like to emphasize with this table (see the caption for more information) is that solution of the elliptic equations is *not* significantly more expensive than the solution of the hyperbolic equations in our model; moreover the scaling of the solution time with problem size is close to linear, again for *both* types of equations. This is not surprising or new in any sense, as one can *immediately* predict this “Golden Rule” scaling behavior from Brandt’s work on multi-level adaptive (MLAT) schemes [46]; indeed, that elliptic equa-

¹¹ The increase in hierarchy depth that occurs when black holes form is partly due to the “grid-stretching” phenomena associated with maximal slicing.

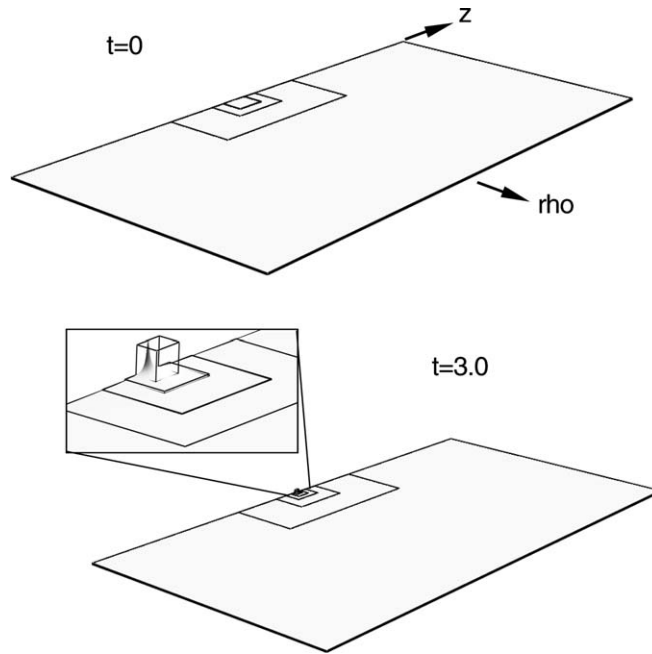


Fig. 9. Surface plots of ψ at $t = 0$ and $t = 3$ from the h adaptive simulation discussed in Section 5.2, where the height of each surface is proportional to the magnitude of ψ (ranging approximately from 1.00 (1.00) at the outer boundary to 1.24 (3.20) at the origin $\rho = z = 0$ at $t = 0$ ($t = 3$)). Overlaid on the surfaces are the AMR grid bounding boxes – there are four levels of 2:1 refinement at $t = 0$, seven levels at $t = 3$, and the base (coarsest) level has a resolution of 257×513 .

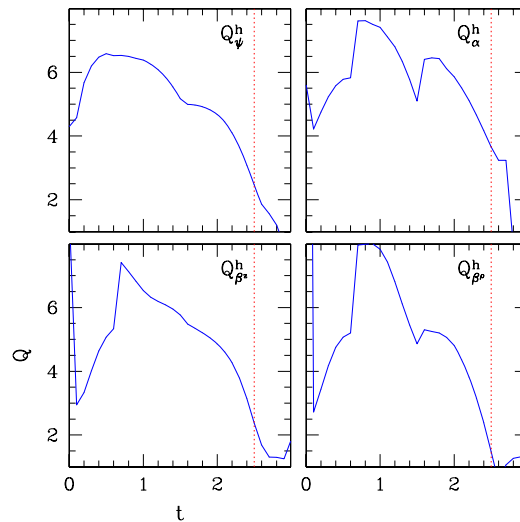


Fig. 10. Convergence factors (13) for the variables ψ , α , β^ρ and β^z , calculated from the fully constrained adaptive simulations discussed in Section 5.2. For second-order accurate finite differencing one would expect $Q \approx 4$. Time symmetric initial data was used in this case, for which the exact solution for β^ρ and β^z at $t = 0$ is 0, hence the anomalous spikes for the corresponding convergence factors then (i.e., $Q \sim 0/0$). A black hole forms at $t \sim 2.5$ (denoted by the dashed vertical line), after which significant gradients in metric functions develop due to the “grid-stretching” property of maximal slicing as the spacetime singularity is first approached, but ultimately avoided; this appears to be the dominant factor causing these three simulations (h , $2h$ and $4h$) to start to depart from the convergent regime (though for any given resolution one expects departure from convergence to eventually occur). We cannot explain why the convergence factor is somewhat greater than four during intermediate times in the simulation, however this is *not* atypical behavior in simulations we have looked at.

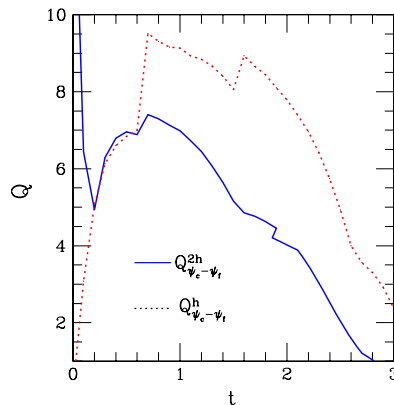


Fig. 11. Convergence factors (15) for the assumed residual quantity $\psi_c - \psi_f$ from the adaptive simulations discussed in Section 5.2, where ψ_c is the conformal factor ψ from the fully constrained simulation, and ψ_f is the conformal factor obtained via free evolution. At $t = 0$ both ψ_f and ψ_c are calculated by solving the Hamiltonian constraint, hence the anomalous behavior in the convergence factor then. Moreover, the boundaries conditions employed are only consistent with the full set of Einstein equations in the limit where the outer boundary position goes to infinity [32]. Early on in the simulation this inconsistency produces a difference in $\psi_c - \psi_f$ that is of the same magnitude as the truncation error of the h simulation, and this causes $Q^h_{\psi_c - \psi_f}$ to start below 4 near $t = 0$. However, as evolution proceeds and gravitational collapse occurs, the gradients in ψ in the central region grow rapidly, and the truncation error component of $Q^h_{\psi_c - \psi_f}$ begins to dominate. As with the results shown in Fig. 10, grid-stretching effects apparently cause the decrease in Q after the black hole forms near $t \sim 2.5$. However, in this plot we can see a trend to improved convergence results at any given time when resolution is increased from Q^{2h} to Q^h .

Table 2

Timing information for the fully constrained simulations described in Section 5.2

Runtime (s)	AMR-4h	AMR-2h	AMR-h
	3.38×10^2	2.00×10^3	1.40×10^4
Percentage of runtime solving elliptics equations	68.2	60.3	50.8
Percentage of runtime solving hyperbolic equations	24.4	33.1	43.1
Percentage of runtime in AMR related functions	3.4	3.4	3.8
Percentage of runtime in miscellaneous functions	4.0	3.2	2.3

The *runtime* is the wall time taken (on a 2.4 GHz Intel XEON processor), in seconds, for each simulation, including initial data calculation and evolution. For this set of simulations, the total number of grid points in space and time (compare Table 1) increases by a factor of 8 from the 4h to 2h simulation, and again by a factor of 8 from the 2h to h simulation. Hence the runtime should increase by a corresponding factor for an algorithm whose cost scales linearly with the number of points – we do, approximately, see this behavior. The next four rows give a rough breakdown of the percentage of total time spent in each of the key parts of the program (calculated using the function profiling option of Portland Group’s *pg* compilers). The two main points we want to stress with this data is that the scaling (with problem size) of the adaptive multigrid algorithm used to solve the elliptic equations is close to *linear*, and is *not* significantly slower than the solution of the hyperbolic equations. Second, the cost of AMR related functions (including regridding, truncation error estimate calculation, interpolation and injection functions) is quite small compared to the cost of solving the numerical equations. The miscellaneous functions of the last row include calculations of diagnostic quantities, the cost of the apparent horizon finder (that searches for the presence of black holes), and I/O.

tions could be solved in linear time within the context of general relativity was already demonstrated in the early 1980s [48,49].

6. Conclusions

In this paper we have discussed modifications of the standard Berger and Olinger adaptive mesh refinement method, so that the resulting algorithm can solve systems resulting from the discretization of *coupled, non-linear, hyperbolic and elliptic equations* in *linear time*. Moreover, as we have retained recursive time-stepping, the algorithm is still optimally efficient in solving systems that contain hyperbolic equations which

are subject to a CFL stability condition. The initial application that drove development of the method was a study of critical gravitational collapse of the scalar field in axisymmetry [32,11,12]. This involved the approximate solution of a mixed elliptic/hyperbolic system: the coupled Einstein–Klein Gordon system in a certain coordinate system, with a particular choice among the overdetermined set of PDEs at our disposal to advance the solution in time. However, the algorithm is sufficiently general that it can be applied to a variety of similar systems of partial differential equations. For example, there are numerous problems in astrophysics that need to evolve various matter equations coupled to gravity and/or the electromagnetic field, including cosmological structure formation, stellar evolution, supernovae, jets, accretion disks, etc. Many of these scenarios have a large range of spatio-temporal length scales that need to be modeled, and can benefit tremendously from Berger and Olinger style AMR. In some situations Newtonian gravity is sufficient to accurately describe the physics, and due to the linearity of the Poisson equation, modifications to Berger and Olinger as described here are not strictly necessary. However, some of the most interesting astrophysical events occur in regions where gravity is sufficiently strong that non-linear effects become important, and the algorithm described in this paper could be of significant use in such simulations.¹²

With regards to new applications of this algorithm in numerical relativity, of particular interest is constrained evolution in 3D, which, on the basis of substantial 1D and 2D evidence [50–56,7,57,58,10,13,61,62,32,11,63,12], we have long felt has great potential for the study of problems such as black hole collisions, critical gravitational collapse, and the structure of black hole interiors. All of the aforementioned lower dimensional studies made use of the symmetries in the problem, in addition to particular coordinate choices, to obtain well-posed coupled elliptic/hyperbolic systems, and so there is some skepticism in the community about whether constrained evolution can be implemented for general problems in 3D. Though recently a fully constrained 3D evolution scheme was proposed in [38], based on the Dirac gauge and spherical coordinates (the implementation presented in [38] made use of a multidomain spectral solution method). A potential disadvantage of this system is that it is not obvious how to generalize it beyond spherical coordinates, which are not well adapted to studying problems that are far from spherical symmetry. A formulation of the Einstein equations that is amenable to 3D constrained evolution and *can* be written in Cartesian coordinates was described in [64]. Both of these formulations are prime candidates for numerical implementation using our AMR algorithm.

Acknowledgments

F.P. thanks Bernd Brügmann for helpful suggestions on an earlier version of the manuscript. The authors gratefully acknowledge research support from CIAR, NSERC, NSF PHY-0099568, NSF PHY-0244906, and Caltech’s Richard Chase Tolman Fund. The simulations described here were performed on UBC’s *vn* cluster (supported by CFI and BCKDF), and the *MACI* cluster at the University of Calgary (supported by CFI and ASRA).

Appendix A. Equations and finite difference operators

Here, for completeness, we list all of the equations introduced in Section 2, and the specific set of finite difference operators used to discretize them.

A.1. Equations

Summarizing Section 2, the four-metric is

$$ds^2 = (-\alpha^2 + \psi^4[(\beta^\rho)^2 + (\beta^z)^2])dt^2 + 2\psi^4(\beta^\rho d\rho + \beta^z dz)dt + \psi^4(d\rho^2 + dz^2 + \rho^2 e^{2\rho\sigma} d\phi^2). \quad (\text{A.1})$$

¹² We note that even the conformally flat approximation to the field equations, which seems to be an adequate extension of Newtonian gravity for a certain class of problems [59,60], requires solution of a non-linear elliptic equation.

The conjugate variable to the scalar field Φ is Π (A.8), and the conjugate to $\bar{\sigma}$ is $\bar{\Omega}$ (6). All of these variables are functions of ρ , z and t . The maximal slicing condition results in the following elliptic equation for α :

$$2(\rho\alpha_{,\rho})_{,\rho^2} + \alpha_{,zz} + \alpha_{,\rho} \left(2\frac{\psi_{,\rho}}{\psi} + (\rho\bar{\sigma})_{,\rho} \right) + \alpha_{,z} \left(2\frac{\psi_{,z}}{\psi} + (\rho\bar{\sigma})_{,z} \right) - \frac{\psi^4}{2\alpha} [(\beta_{,\rho}^\rho - \beta_{,z}^z)^2 + (\beta_{,z}^\rho + \beta_{,\rho}^z)^2] - \frac{\psi^4}{6\alpha} [2\alpha\rho\bar{\Omega} + \beta_{,\rho}^\rho - \beta_{,z}^z]^2 - 16\pi\alpha\Pi^2 = 0. \quad (\text{A.2})$$

The Hamiltonian constraint is

$$8\frac{\psi_{,\rho\rho}}{\psi} + 8\frac{\psi_{,zz}}{\psi} + 16\frac{\psi_{,\rho^2}}{\psi} + 8(\rho\bar{\sigma})_{,\rho} \frac{\psi_{,\rho}}{\psi} + 8(\rho\bar{\sigma})_{,z} \frac{\psi_{,z}}{\psi} + \frac{\psi^4}{2\alpha^2} [(\beta_{,\rho}^\rho - \beta_{,z}^z)^2 + (\beta_{,\rho}^z + \beta_{,z}^\rho)^2] + \frac{\psi^4}{6\alpha^2} [2\alpha\rho\bar{\Omega} + \beta_{,\rho}^\rho - \beta_{,z}^z]^2 = -16\pi(\Pi^2 + \Phi_{,\rho}^2 + \Phi_{,z}^2) - 6(\rho^2(\rho\bar{\sigma})_{,\rho})_{,\rho^3} - 2((\rho\bar{\sigma})_{,\rho})^2 - 2(\rho\bar{\sigma})_{,zz} - 2((\rho\bar{\sigma})_{,z})^2. \quad (\text{A.3})$$

The ρ and z momentum constraints are

$$\frac{2}{3}\beta_{,\rho\rho}^\rho + \beta_{,zz}^\rho + \frac{1}{3}\beta_{,z\rho}^z + 32\pi\frac{\alpha}{\psi^2}\Pi_{,\rho} - \left(\left(\frac{\alpha_{,z}}{\alpha} - 6\frac{\psi_{,z}}{\psi} \right) - (\rho\bar{\sigma})_{,z} \right) (\beta_{,\rho}^z + \beta_{,z}^\rho) - \frac{2}{3} \left(\frac{\alpha_{,\rho}}{\alpha} - 6\frac{\psi_{,\rho}}{\psi} \right) [\beta_{,\rho}^\rho - \beta_{,z}^z] - \frac{8}{3}\alpha\bar{\Omega} - \frac{2\alpha\rho}{3} \left[6\bar{\Omega}\frac{\psi_{,\rho}}{\psi} + \bar{\Omega}_{,\rho} + 3\bar{\Omega}(\rho\bar{\sigma})_{,\rho} \right] = 0, \quad (\text{A.4})$$

and

$$\beta_{,\rho\rho}^z + \frac{4}{3}\beta_{,zz}^z - \frac{1}{3}\beta_{,z\rho}^\rho + \left[(\rho\bar{\sigma})_{,\rho} + \frac{2\alpha}{\psi^6} \left(\frac{\rho\psi^6}{\alpha} \right)_{,\rho^2} \right] (\beta_{,z}^\rho + \beta_{,\rho}^z) + \left[2(\rho\bar{\sigma})_{,z} - \frac{4}{3} \left(\frac{\alpha_{,z}}{\alpha} - 6\frac{\psi_{,z}}{\psi} \right) \right] (\beta_{,z}^z - \beta_{,\rho}^\rho) - \frac{2\alpha\rho}{3} \left(6\bar{\Omega}\frac{\psi_{,z}}{\psi} + \bar{\Omega}_{,z} \right) + 32\pi\frac{\alpha}{\psi^2}\Pi_{,z} - 2\alpha(\bar{\sigma}_{,z})\rho^2\bar{\Omega} = 0. \quad (\text{A.5})$$

The definition of $\bar{\Omega}$ (6) gives an evolution equation for $\bar{\sigma}$:

$$\bar{\sigma}_{,t} = 2\beta^\rho(\rho\bar{\sigma})_{,\rho^2} + \beta^z\bar{\sigma}_{,z} - \alpha\bar{\Omega} - \left[\frac{\beta^\rho}{\rho} \right]_{,\rho}. \quad (\text{A.6})$$

The evolution equation for $\bar{\Omega}$ is

$$\bar{\Omega}_{,t} = 2\beta^\rho(\rho\bar{\Omega})_{,\rho^2} + \beta^z\bar{\Omega}_{,z} - \frac{1}{2\alpha\rho}(\beta_{,\rho}^{z^2} - \beta_{,z}^{\rho^2}) + \frac{1}{\psi^4} \left(\frac{\alpha_{,\rho}}{\rho} \right)_{,\rho} + \frac{\alpha}{\psi^6} \left(\frac{(\psi^2)_{,\rho}}{\rho} \right)_{,\rho} - \frac{2\alpha}{\psi^4} \left(4\frac{\psi_{,\rho^2}}{\psi} + (\rho\bar{\sigma})_{,\rho^2} \right) \left(\frac{\alpha_{,\rho}}{\alpha} + \frac{2\psi_{,\rho}}{\psi} \right) - \frac{\alpha}{\psi^4} \left[\bar{\sigma}_{,z} \left(\frac{\alpha_{,z}}{\alpha} + \frac{2\psi_{,z}}{\psi} \right) + \rho\bar{\sigma}_{,z}^2 + \bar{\sigma}_{,zz} \right] + 64\pi\frac{\alpha}{\psi^4}\rho(\Phi_{,\rho^2})^2. \quad (\text{A.7})$$

The definition of Π and the wave equation for Φ give

$$\Phi_{,t} = \beta^\rho\Phi_{,\rho} + \beta^z\Phi_{,z} + \frac{\alpha}{\psi^2}\Pi, \quad (\text{A.8})$$

and

$$\Pi_{,t} = \beta^\rho\Pi_{,\rho} + \beta^z\Pi_{,z} + \frac{1}{3}\Pi(\alpha\rho\bar{\Omega} + 2\beta_{,\rho}^\rho + \beta_{,z}^z) + \frac{1}{\psi^4} [2(\rho\alpha\psi^2\Phi_{,\rho})_{,\rho^2} + (\alpha\psi^2\Phi_{,z})_{,z}] + \frac{\alpha}{\psi^2} [(\rho\bar{\sigma})_{,\rho}\Phi_{,\rho} + (\rho\bar{\sigma})_{,z}\Phi_{,z}]. \quad (\text{A.9})$$

The maximal slicing condition $K = 0$ gives an independent hyperbolic evolution equation for ψ :

$$\psi_{,t} = \psi_{,z}\beta^z + \psi_{,\rho}\beta^\rho + \frac{\psi}{6}(2\beta_{,\rho}^\rho + \beta_{,z}^z + \rho\alpha\bar{\Omega}). \quad (\text{A.10})$$

A.2. Boundary conditions

The set of axis regularity conditions, applied at $\rho = 0$ are:

$$\begin{aligned}
 \alpha_{,\rho} &= 0, \\
 \psi_{,\rho} &= 0, \\
 \beta^z_{,\rho} &= 0, \\
 \beta^\rho &= 0, \\
 \bar{\sigma} &= 0, \\
 \bar{\Omega} &= 0, \\
 \Phi_{,\rho} &= 0, \\
 \Pi_{,\rho} &= 0.
 \end{aligned}
 \tag{A.11}$$

The outer boundary conditions used, applied at $\rho = \rho_{\max}$, $z = z_{\max}$ and $z = z_{\min}$, are:

$$\begin{aligned}
 \alpha &= 1, \\
 \psi - 1 + \rho\psi_{,\rho} + z\psi_{,z} &= 0, \\
 \beta^z &= 0, \\
 \beta^\rho &= 0, \\
 r\bar{\sigma}_{,t} + \rho\bar{\sigma}_{,\rho} + z\bar{\sigma}_{,z} + \bar{\sigma} &= 0, \\
 r\bar{\Omega}_{,t} + \rho\bar{\Omega}_{,\rho} + z\bar{\Omega}_{,z} + \bar{\Omega} &= 0, \\
 r\Phi_{,t} + \rho\Phi_{,\rho} + z\Phi_{,z} + \Phi &= 0, \\
 r\Pi_{,t} + \rho\Pi_{,\rho} + z\Pi_{,z} + \Pi &= 0.
 \end{aligned}
 \tag{A.12}$$

A.3. Finite difference operators

In this section, we write out all of the difference operators used to convert the differential equations in the previous section to finite difference equations. At all interior points of the mesh, the centered forms of the derivative operators are used, and along boundaries, backward and forward operators are used as appropriate. Kreiss–Oliger style dissipation is applied to evolution equations, at interior points at least two grid points inward, in the direction of the stencil, from any boundary. For $\bar{\sigma}$ and $\bar{\Omega}$, we linearly interpolate in ρ at location $\Delta\rho$ (and optionally at $2\Delta\rho$ as well), using the values of these variables at $\rho = 0$ and $\rho = 2\Delta\rho$ (or $\rho = 3\Delta\rho$). Below, we use the notation $u_{i,j}$ to label a point in the mesh corresponding to coordinate location $(i - 1)\Delta\rho$, $z_{\min} + (j - 1)\Delta z$ (except for the coordinate variable ρ , where it is sufficient to use ρ_i). For time derivatives, we use $u_{i,j}^n$ to denote the retarded time level, and $u_{i,j}^{n+1}$ the advanced time level. All of the finite-difference operators are second-order accurate.

A.3.1. Centered difference operators

$$u_{,\rho} \rightarrow \frac{u_{i+1,j} - u_{i-1,j}}{2\Delta\rho},
 \tag{A.13}$$

$$u_{,z} \rightarrow \frac{u_{i,j+1} - u_{i,j-1}}{2\Delta z},
 \tag{A.14}$$

$$u_{,\rho\rho} \rightarrow \frac{u_{i+1,j} - 2u_{i,j} + u_{i-1,j}}{(\Delta\rho)^2},
 \tag{A.15}$$

$$u_{,zz} \rightarrow \frac{u_{i,j+1} - 2u_{i,j} + u_{i,j-1}}{(\Delta z)^2},
 \tag{A.16}$$

$$u_{,\rho^2} \rightarrow \frac{u_{i+1,j} - u_{i-1,j}}{\rho_{i+1}^2 - \rho_{i-1}^2}, \quad (\text{A.17})$$

$$(u/\rho)_{,\rho} \rightarrow \frac{u_{i+1,j} + u_{i,j}}{2\Delta\rho(\rho_i + \Delta\rho/2)} - \frac{u_{i,j} + u_{i-1,j}}{2\Delta\rho(\rho_i - \Delta\rho/2)}, \quad (\text{A.18})$$

$$(u_{,\rho}/\rho)_{,\rho} \rightarrow \frac{u_{i+1,j} - u_{i,j}}{(\Delta\rho)^2(\rho_i + \Delta\rho/2)} - \frac{u_{i,j} - u_{i-1,j}}{(\Delta\rho)^2(\rho_i - \Delta\rho/2)}, \quad (\text{A.19})$$

$$u_{,t} \rightarrow \frac{u_{i,j}^{n+1} - u_{i,j}^n}{\Delta t}. \quad (\text{A.20})$$

A.3.2. Forward-difference operators

$$u_{,\rho} \rightarrow \frac{-u_{i+2,j} + 4u_{i+1,j} - 3u_{i,j}}{2\Delta\rho}, \quad (\text{A.21})$$

$$u_{,z} \rightarrow \frac{-u_{i,j+2} + 4u_{i,j+1} - 3u_{i,j}}{2\Delta z}. \quad (\text{A.22})$$

A.3.3. Backward-difference operators

$$u_{,\rho} \rightarrow \frac{u_{i-2,j} - 4u_{i-1,j} + 3u_{i,j}}{2\Delta\rho}, \quad (\text{A.23})$$

$$u_{,z} \rightarrow \frac{u_{i,j-2} - 4u_{i,j-1} + 3u_{i,j}}{2\Delta z}. \quad (\text{A.24})$$

A.3.4. Dissipation operators

The following dissipation operator is applied in the ρ direction:

$$\frac{\epsilon_d}{16} (u_{i-2,j} - 4u_{i-1,j} + 6u_{i,j} - 4u_{i+1,j} + u_{i+2,j}) \quad (\text{A.25})$$

and in the z direction:

$$\frac{\epsilon_d}{16} (u_{i,j-2} - 4u_{i,j-1} + 6u_{i,j} - 4u_{i,j+1} + u_{i,j+2}), \quad (\text{A.26})$$

where $0 \leq \epsilon_d \leq 1$.

Appendix B. Additional algorithm details

This appendix contains descriptions of a few additional features of the AMR algorithm described in the paper: computing TE estimates using a self-shadow hierarchy, details of how the multigrid algorithm is applied to an adaptive hierarchy, and a description of the particular set of interpolation and restriction operators used.

B.1. A self-shadow hierarchy for computing truncation error estimates

A self-shadow hierarchy is a simplification of the idea of using a *shadow hierarchy* to do truncation error estimation. A shadow hierarchy is a coarsened (usually with $\rho_s = 2:1$ version of the main hierarchy). Both hierarchies are evolved simultaneously, and the function values of a given grid in the shadow hierarchy are replaced with those of the corresponding grid in the main hierarchy whenever the two are in sync. For example, with $\rho_t = 2:1$, each time step of a shadow grid corresponds to two time steps of the main grid, and the shadow is updated every two main-grid time steps. A TE estimate can therefore readily be computed by comparing function values in the shadow with corresponding values in the main hierarchy just before the update step.

Notice however, that within the recursive time-stepping flow of the Berger and Olinger algorithm, information for computing a TE estimate is “naturally” available prior to the fine-to-coarse grid injection step (see Fig. 4). The coarse level ℓ is evolved independently of the fine level $\ell + 1$ from t_0 to $t_0 + \Delta t_c$, where Δt_c is the coarse level time step. Also, at $t = t_0$ the level ℓ grid functions are restricted copies of level $\ell + 1$ grid functions in the region of overlap $O_\ell^{\ell+1}$. Therefore, prior to injection at time $t_0 + \Delta t_c$, the difference in an evolved variable f in levels ℓ and $\ell + 1$, within the region $O_\ell^{\ell+1}$, can serve as an approximation to the truncation error $\tau_s(f_{\ell+1})$ for f at level $\ell + 1$:¹³

$$\tau_s(f_{\ell+1}) \equiv f_{\ell+1} - f_\ell. \tag{B.1}$$

Therefore, for levels $\ell > 1$, one can use (B.1) as the basis for computing truncation error estimates, without the need to refer to a shadow hierarchy (i.e., the main hierarchy “casts its own shadow”, hence the name self-shadow hierarchy). This method cannot give a TE estimate for the coarsest level (1) in the hierarchy, and so we require that the coarsest level always be fully refined. Thus, the resolution of level 2 is chosen to match the desired coarsest resolution for a given problem (for the sample evolutions described in Section 5, level 2 is always quoted as the base level).

In practice, a slightly modified form of B.1 is used, as we now describe. Depending upon the problem, one or more of ψ , Φ , Π_Φ , $\bar{\Omega}$, and $\bar{\sigma}$ are used in the calculation (i.e., all evolved quantities – ψ is not used when the Hamiltonian constraint is used to solved for ψ in a fully constrained evolution). Optionally, the truncation error estimate is scaled by the norm of the function, if the norm is larger than some constant k ($k = 1$ typically), and can also be multiplied by ρ^p , for some integer p chosen heuristically to either enhance or reduce the near-axis refinement. The TE estimate for a function f_ℓ at level ℓ is thus defined to be

$$\tau_s(f_\ell) = \frac{(f_\ell - f_{\ell-1})\rho^p}{\max(k, \|f_\ell\|_2)}, \tag{B.2}$$

where it is implied that f_ℓ is only defined in the overlap between levels ℓ and $\ell - 1$, f_ℓ is restricted to the resolution of level $\ell - 1$ prior to subtraction, and the result is then interpolated back to the resolution of level ℓ . Typically, we use $p = 2$ for $\bar{\Omega}$, $p = 1$ for $\bar{\sigma}$, and $p = 0$ for the other variables. The TE estimate for the level is defined to be

$$\tau_s(\ell) = \sqrt{\sum \tau_s(f_\ell)^2}, \tag{B.3}$$

where the sum is taken over the desired subset of variables listed above.

Optionally, the TE estimate calculated in (B.3) is further smoothed (using simple averaging over a 5-by-5 square cell of points), and/or scaled by a quantity $H_\ell \geq 1$ in the region of overlap between levels ℓ and $\ell + 1$. H_ℓ therefore provides a kind of “hysteresis” to the truncation error estimation process: when the TE estimate in a region of level ℓ grows above τ_{\max} , that region is refined; however, for the region to be unrefined at a later time, the TE estimate needs to drop below τ_{\max}/H_ℓ there. In most of the simulations we keep $H_\ell = 1$, though occasionally it has proven useful to set it to around 5–10.

B.2. Multigrid on an adaptive hierarchy

The FAS multigrid algorithm, with V-cycling, that we use to solve elliptic equations on a grid hierarchy such as that shown in Fig. 2 is based on Brandt’s multi level adaptive (MLAT) scheme [46], and is similar to that used in [25]. To simplify the algorithm, we require that $\rho_s = 2^q$ for some integer q ; then the AMR hierarchy can easily be extended to incorporate the multigrid levels, which have a refinement ratio ρ_{mg} of 2:1. When building the multigrid hierarchy, each AMR grid is individually coarsened by factors ρ_{mg} (i.e., factors of 2) until either (a) one dimension of the grid is smaller than the minimum allowed, or (b) the coarsened grid can be “absorbed” into a larger grid at that level in hierarchy. With this type of hierarchy the V-cycle begins

¹³ In fact, if there are only two levels in the hierarchy, then this estimate is exactly the truncation error estimate one would obtain with a shadow hierarchy. If levels finer than $\ell + 1$ exist, then in the overlap $O_{\ell+1}^{\ell+2}$ the estimate (B.1) will be modified by an amount of order $(\Delta t_c/\rho_s)^2$.

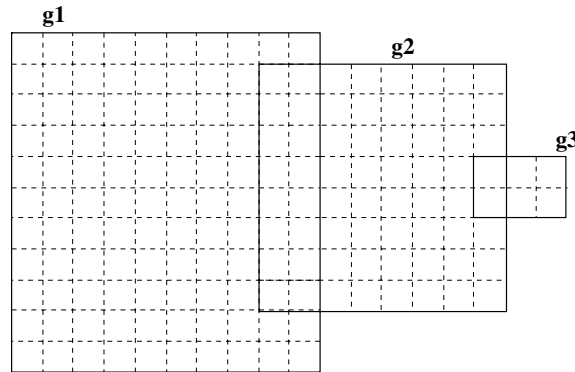


Fig. 12. A hypothetical multigrid grid configuration that will adversely affect execution speed. In the figure we depict three grids, g_1 , g_2 and g_3 , several levels down in the grid hierarchy (i.e., after several coarsening steps have already been performed). Grid g_3 cannot be coarsened any further, while grids g_1 and g_2 can, and ideally should be coarsened further, to maintain the speed of the algorithm. However, because g_3 overlaps the other two grids, this entire level must be considered a coarsest level, and solved “exactly”.

with relaxation of the finest level grids only. Then as the finer levels are coarsened they are absorbed, if possible, into coarser levels. This method of relaxation on an adaptive hierarchy is in contrast to the fast adaptive composite grid method [65], though we do not believe that the particular details of how the elliptic equations are solved have much bearing on the algorithm described here for dealing with coupled elliptic/hyperbolic equations.

A couple of minor points regarding the details of the multigrid solution are worth mentioning. First, inter-level operations, such as restriction, computing coarse-grid corrections, etc., are only performed in the region of overlap between the two levels (which is *always* the region of the fine level, given the kind of hierarchies that are produced by B&O AMR). Second, the manner in which the relaxation sweep proceeds over a level is modified, to account for possible grid overlap,¹⁴ as follows. During the relaxation sweep, the variables at a given coordinate location and level are relaxed *only once*, regardless of the number of grids encompassing that location. This is crucial in order to preserve the smoothing properties of the relaxation scheme. We use a mask function to enforce this requirement of a single update per grid point. The mask is initialized to zero on all grids at that level, prior to a relaxation sweep. Then, on a given level, a sweep is applied, in turn, to each grid in the level, but only variables at points where the mask is equal to zero are modified. After the sweep is complete on a given grid, the mask is set to one throughout the grid, and the mask and other grid functions are copied to overlapping grids at the same level. Therefore, subsequent relaxation sweeps on adjacent grids skip over points that have already been relaxed. This communication step, in addition to enforcing a single update per point, ensures that grid functions are numerically unique at all physical grid locations,¹⁵ which is important for preserving the convergence properties of multigrid. Also, although Dirichlet boundary conditions are used at interior boundaries (i.e., those not abutting boundaries of the computational domain) of any single grid, the communication ensures that points interior to a union of grids are ultimately updated using the PDEs, even if they lie on the boundary of some grid in the overlap region.

With regards to the performance of this multigrid scheme on a general adaptive hierarchy, there are two situations of relevance where performance could suffer, compared to the single grid multigrid algorithm. The first occurs when, at some level down (coarser) in the multigrid hierarchy, one or more grids in a connected union of grids is a “coarsest grid”, and hence needs to be solved “exactly”¹⁶ – see Fig. 12.

¹⁴ We require that grids at the same level *must* overlap when spanning a connected region of the computational domain. In other words, it is not sufficient for grids to merely “touch” at a common boundary between them. This requirement simplifies the relaxation subroutine so that it can operate locally on a grid-by-grid basis, without needing to communicate adjacent information. However, as described in the text, the communication step then needs to be shifted to other parts of the algorithm.

¹⁵ Note that such a communication step is also performed after relaxation of evolved variables, during the Crank–Nicholson iteration.

¹⁶ Here, “exactly” means that the residual on the coarsest grid is reduced by several orders of magnitude by relaxation (it is usually not necessary to solve the coarse-grid problem to within machine precision).

Experimentation showed that the *entire union* needs to be solved exactly in that situation; i.e., it is not sufficient to solve the equations exactly on the coarsest grids, then proceed down the V-cycle on the remaining grids. If the union of grids consists of a relatively small number of grid points, then such a situation will not be a problem; otherwise, there will be a significant slow-down of the code, for the speed of an exact solve suffers dramatically as the number of unknowns increase. To date, we have been able to avoid this potential speed bottleneck by using a more simplistic clustering method that does not produce grid-overlap, as discussed in the following section.

The second situation where performance suffers is when the TE estimate requires long, skinny rectangular regions to be refined. This does occur with the more prolate initial data configurations that have been studied [43]. What happens then, is that such an elongated grid can not be coarsened very much along the larger grid dimension before the smaller dimension has reached the smallest allowed size. Again, this results in a relatively large number of points on the coarsest grid where the solution needs to be obtained exactly. As of yet this problem has not been addressed.

B.3. Clustering

We have incorporated two clustering routines into the code. The first, written by Reid Guenther, Mijan Huq and Dale Choi [66], is based upon the signature-line method of Berger and Rigoutsos [67]. The second is a simple routine that produces single, isolated clusters – each isolated region of high TE is surrounded by a single cluster, and then all clusters within a certain distance of each other are merged together into an encompassing cluster. For the problems studied so far, the isolated cluster method turns out to be almost as efficient as the signature-line method. Therefore, since efficiency is not an issue, the isolated cluster method is preferable, because it avoids one of the potential speed-bottlenecks of the multigrid algorithm discussed in Appendix B.2; furthermore, as mentioned in Appendix B.6, minimizing cluster overlap helps reduce high-frequency noise problems.

A clustering issue that needs to be dealt with in this code is that the resultant grid hierarchy must be compatible with the multigrid solver. This places two restrictions on cluster sizes and positions. First, an individual grid must have dimensions that can be factored into $x_{\min}2^n$, where x_{\min} is one of the smallest, allowed grid dimensions, and n is a non-negative integer. Second, if several grids overlap, then their relative positions must be such that the common grid points align on all possible levels of a multigrid hierarchy. Specifically, if a union of overlapping grids can collectively be coarsened m times in the multigrid hierarchy, then the relative offsets of grid origins on the finest level must be multiples of 2^m grid points. These requirements are enforced after the initial clustering algorithm is called, by modifying the returned cluster list accordingly. This gives more flexibility to experiment with different clustering routines, which consequently do not need to be aware of the alignment issues.

To conclude this section we mentioned a couple of additional options that have been implemented in the post-clustering routine. They are adding “ghost zones” between adjacent, touching clusters, so that both the multigrid and evolution relaxation sweeps correctly solve the system of equations in a domain given by the union of grids at a given level; and optionally moving or shrinking clusters, if necessary, to prevent them from touching parent boundaries,¹⁷ which helps to avoid instabilities that occasionally occur in such situations.

B.4. Interpolation and restriction operators

Here we state the restriction and interpolation operators used in the AMR code. Simple injection is used to restrict a fine grid to a coarse grid during the injection phase of the AMR algorithm, and when computing the TE estimate. A fourth order (bi-cubic) interpolation scheme is used to initialize newly refined fine grids (or regions thereof) from the encompassing coarser grid. The scheme proceeds by first interpolating every row

¹⁷ In principle this should never occur if one adds a buffer zone about the region of high truncation error. However, because of the grid shuffling performed to obtain a hierarchy acceptable to multigrid, a grid could be extended to touch a parent boundary. With the option enabled to prevent this, the grid will be reduced rather than extended to fit into the multigrid scheme. This comes at the expense of not obtaining “optimal” zones about the region of high truncation error.

of the coarse grid to the fine grid (i.e., every ρ_s th row of the fine grid is filled in), then all the remaining points on the fine grid are computed via interpolation, column-by-column. The multigrid routine uses half-weight restriction when transferring from a fine to coarse grid, and linear interpolation for the coarse to fine transfer.

B.5. Initializing the grid hierarchy

Fig. 13 below contains a pseudo-code description of the steps used to initialize the grid hierarchy.

```

t:=0;
initialize the grid hierarchy with 2 levels, each covering the entire domain; (so  $\ell_f = 2$ )

repeat
   $\ell_f^p := \ell_f$ ;
  call set_initial_data(); (see below)
  call set_past_t_data_1st_order(); (see below)
  call single_step(1); (see Fig.4)
  regrid the entire hierarchy using truncation error estimates
    computed in the previous step; (thus possibly changing  $\ell_f$ )
  reset  $t$  to  $t := 0$  while retaining the current hierarchy structure;
until  $\ell_f = \ell_f^p$  or maximum number of refinement levels reached

call set_initial_data();
call set_past_t_data_1st_order();

call single_step(1); (evolve hierarchy forwards in time one coarse step)
call flip_dt; (see below)

call single_step(1); (evolve hierarchy backwards in time one coarse step)
call flip_dt;

call set_initial_data();

(done computing initial data and hierarchy)

subroutine set_initial_data()
  initialize hyperbolic variables over levels [1.. $\ell_f$ ] with freely-specifiable data;
  solve the elliptic equations over levels [1.. $\ell_f$ ];
end of subroutine set_initial_data

subroutine flip_dt()
  for each elliptic variable  $f_1(t)$ :  $f_1(t + \Delta t_1) := 2f_1(t) - f_1(t - \Delta t_1)$ ;
  do  $\ell := 2$  to  $\ell_f$ 
    for each elliptic variable  $f_\ell(t)$ :  $f_\ell(t + \rho_t \Delta t_\ell) := 2f_\ell(t) - f_\ell(t - \rho_t \Delta t_\ell)$ ;
     $\Delta t_\ell := -\Delta t_\ell$ ;
  end do
end of subroutine flip_dt

subroutine set_past_t_data_1st_order()
  do  $\ell := 1$  to  $\ell_f$ 
    for each elliptic variable  $f_\ell(t)$ :  $f_\ell(t - \rho_t \Delta t_\ell) := f_\ell(t)$ ;
  end do
end of subroutine set_past_t_data_1st_order

```

Fig. 13. A pseudo-code description of the steps we use to initialize the grid hierarchy. The *repeat* loop is used to calculate the hierarchy structure at $t = 0$. Then, to initialize past time level data for elliptic variables using linear extrapolation (which is done in *flip_dt*()), the entire hierarchy is evolved forwards, then backwards in time by single coarse level time steps (alternatively we could evolve backwards, then forwards in time here – the results would essentially be the same). The idea behind this last step is that since the evolution of the hyperbolic variables is driving any change in the elliptic variables, we can use the results of a small evolution step to provide a better estimate of past time level information than first-order extrapolation of the solution at $t = 0$. In principle, this step can be iterated if need be, though we found that a single step is sufficient (though *not* always necessary depending on the free initial data) to obtain close to second-order convergence of the final solution.

B.6. Controlling high-frequency grid-boundary noise

An issue that needs to be dealt with in a Berger & Olinger style AMR scheme is controlling high-frequency solution components (“noise”) that may occur at parent–child grid boundaries. For a second-order accurate finite-difference scheme, the second derivatives of grid functions are typically not continuous across the boundaries after child to parent injection. This potential source of high-frequency noise on the parent level is rather efficiently eliminated by the Kreiss–Olinger dissipation filters we incorporate into our finite differenced evolution equations.

In certain situations we have found that high-frequency noise also develops on child grids, within a grid point or two of the AMR boundary (in particular near the corners of the grid, or places where two grids overlap). This noise is not as easily dealt with, as the Kreiss–Olinger filter acting normal to the boundary is only applied a distance three points and further away from the boundary. The source of this noise appears to be the parent–child interpolation scheme used to set the boundary values, and in general the interpolation method must be tailored to each variable in order to reduce the noise to an acceptable level. For our current model, we use the following interpolation method. For all evolved variables ($\bar{\sigma}$, $\bar{\Omega}$, Φ , Π_ϕ and ψ) we use linear interpolation in time from the parent level to set boundary values on the child grid at points coincident with parent grid points. This is followed by fourth-order interpolation in space (as described in Appendix B.4) for the remaining boundary points. Furthermore (see Fig. 14 and 15), after each step of the Crank–Nicholson iteration we reset $\bar{\Omega}$ and $\bar{\sigma}$ in a zone two grid points in from AMR boundaries with values obtained either (1) by fourth-order interpolation using function values from the boundary and three additional points inward from this zone, or (2) via bilinear interpolation at “corner” points, i.e., those points that are a single cell width away from two boundaries. This technique for $\bar{\sigma}$ and $\bar{\Omega}$ was discovered after quite a bit of experimentation with different interpolation schemes, and is quite effective in reducing the level of noise at the grid boundaries.

For the elliptic variables (α , β^p , β^z and optionally ψ), prior to a Crank–Nicholson evolution cycle, we reset these variables on AMR boundaries at points unique to the grid (in between points coincident with parent level points – those labeled by (2) in Fig. 14) using fourth-order interpolation from the remaining points on the boundary. This overwrites the values set by coarse-grid corrections (CGCs) during the most recent multigrid solve that involved coarser levels. The reason for doing this is as follows. In multigrid, CGCs typically introduce high-frequency noise on the finer level, while the subsequent post-CGC relaxation sweeps smooth out this noise. However, since no relaxation is applied on AMR boundaries, some form of explicit smoothing is required – the above described fourth-order interpolation provides this smoothing mechanism.

Another stage in the algorithm where high-frequency noise can creep into the solution is during the regrid-
ding phase, if the refined region on a given level expands. Then, within the part of a new grid overlapping the

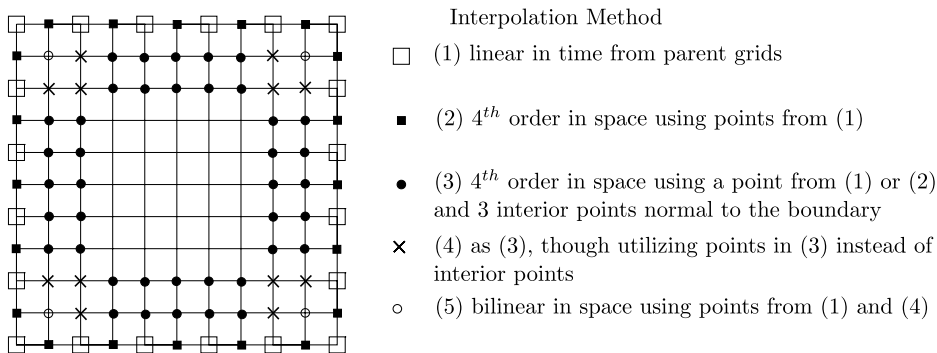


Fig. 14. An illustration of the interpolation method used for $\bar{\sigma}$ and $\bar{\Omega}$ during AMR evolution. In the figure we assume that the spatial refinement ratio is 2:1, and that all four grid boundaries are AMR boundaries. Points labeled by (1) and (2) are set once prior to the Crank–Nicholson (CN) iteration, while points labeled by (3)–(5) are reset after every CN step (see the pseudo-code in Fig. 15). Points not explicitly labeled are “interior” points, and are evolved.

```

subroutine interp_interior_AMR_bnd(grid function f[1..Nrho,1..Nz])
  for i=3 to Nrho-2 do
    f(i,2)=0.4*f(i,1)+2.0*f(i,4)-2.0*f(i,5)+0.6*f(i,6)
    f(i,3)=0.1*f(i,1)+2.0*f(i,4)-1.5*f(i,5)+0.4*f(i,6)
    f(i,Nz-1)=0.4*f(i,Nz)+2.0*f(i,Nz-3)-2.0*f(i,Nz-4)+0.6*f(i,Nz-5)
    f(i,Nz-2)=0.1*f(i,Nz)+2.0*f(i,Nz-3)-1.5*f(i,Nz-4)+0.4*f(i,Nz-5)
  end do

  for j=3 to Nz-2 do
    f(2,j)=0.4*f(1,j)+2.0*f(4,j)-2.0*f(5,j)+0.6*f(6,j)
    f(3,j)=0.1*f(1,j)+2.0*f(4,j)-1.5*f(5,j)+0.4*f(6,j)
    f(Nrho-1,j)=0.4*f(Nrho,j)+2.0*f(Nrho-3,j)-2.0*f(Nrho-4,j)+0.6*f(Nrho-5,j)
    f(Nrho-2,j)=0.1*f(Nrho,j)+2.0*f(Nrho-3,j)-1.5*f(Nrho-4,j)+0.4*f(Nrho-5,j)
  end do

  f(2,2)=(f(1,1)+f(3,3)+f(1,3)+f(3,1))/4
  f(Nrho-1,2)=(f(Nrho,1)+f(Nrho,3)+f(Nrho-2,1)+f(Nrho-2,3))/4
  f(2,Nz-1)=(f(1,Nz)+f(3,Nz)+f(1,Nz-2)+f(3,Nz-2))/4
  f(Nrho-1,Nz-1)=(f(Nrho,Nz)+f(Nrho,Nz-2)+f(Nrho-2,Nz)+f(Nrho-2,Nz-2))/4

end of subroutine interp_interior_AMR_bnd

```

Fig. 15. A pseudo-code description of part of the interpolation method used for $\bar{\sigma}$ and $\bar{\Omega}$ during AMR evolution. For simplicity, in this subroutine we assume that all four boundaries are interior to the computational domain boundaries. The set of points altered here correspond to (3)–(5) in Fig. 14, and the interpolation operators used are independent of the spatial refinement ratio (as opposed to points (1) and (2) in Fig. 14).

old refined region, grid functions will be initialized by copying data from an old fine grid, while on the remaining part of the new grid the grid functions will be initialized via interpolation from a parent grid. Sometimes, at the interface between the copied/interpolated data, tiny discontinuities are introduced. The grid functions are then easily smoothed by applying a Kreiss–Oliger filter to them (at all time levels involved) after regriding.

References

- [1] L. Lehner, Numerical relativity: a review, *Class. Quant. Grav.* 18 (2001) R25.
- [2] C. Gundlach, Critical phenomena in gravitational collapse, *Living Rev. Rel.* 2 1999-4.
- [3] B. Berger, Numerical Approaches to Spacetime Singularities, *Living Rev. Rel.* 2002-1.
- [4] L. Smarr, The Structure of General Relativity with a Numerical Illustration: The Collision of Two Black Holes, University of Texas at Austin Ph.D. thesis, 1975.
- [5] B. Brüggmann, W. Tichy, N. Jansen, Numerical simulation of orbiting black holes, *Phys. Rev. Lett.* 92 (2004) 211101.
- [6] M.D. Duez, P. Marronetti, S.L. Shapiro, T.W. Baumgarte, Hydrodynamic simulations in 3 + 1 general relativity, *Phys. Rev. D* 67 (2003) 024004.
- [7] M.W. Choptuik, Universality and scaling in gravitational collapse of a massless scalar field, *Phys. Rev. Lett.* 70 (1993) 9.
- [8] R.S. Hamade, J.M. Stewart, The spherically symmetric collapse of a massless scalar field, *Class. Quant. Grav.* 13 (1996) 497.
- [9] R.S. Hamade, J.H. Horne, J.M. Stewart, Continuous self-similarity and S-duality, *Class. Quant. Grav.* 13 (1996) 2241.
- [10] M.W. Choptuik, T. Chmaj, P. Bizon, Critical behaviour in gravitational collapse of a Yang–Mills field, *Phys. Rev. Lett.* 77 (1996) 424.
- [11] M.W. Choptuik, E.W. Hirschmann, S.L. Liebling, F. Pretorius, Critical collapse of the massless scalar field in axisymmetry, *Phys. Rev. D* 68 (2003) 044007.
- [12] M.W. Choptuik, E.W. Hirschmann, S.L. Liebling, F. Pretorius, Critical collapse of a complex scalar field with angular momentum, *Phys. Rev. Lett.* 93 (2004) 131101.
- [13] S.L. Liebling, M.W. Choptuik, Black hole criticality in the Brans–Dicke model, *Phys. Rev. Lett.* 77 (1996) 1424.
- [14] M.W. Choptuik, E.W. Hirschmann, S.L. Liebling, Instability of an ‘Approximate Black Hole’, *Phys. Rev. D* 55 (1997) 6014.
- [15] S.L. Liebling, The singularity threshold of the nonlinear sigma model using 3D adaptive mesh refinement, *Phys. Rev. D* 66 (2002) 041703.
- [16] S. Hern, Numerical Relativity and Inhomogeneous Cosmologies, PhD dissertation, Cambridge, gr-qc/0004036, 1999.
- [17] B. Brüggmann, Adaptive mesh and geodesically sliced Schwarzschild spacetime in 3 + 1 dimensions, *Phys. Rev. D* 54 (1996) 7361.
- [18] P. Papadopoulos, E. Seidel, L. Wild, Adaptive computation of gravitational waves from black hole interactions, *Phys. Rev. D* 58 (1998) 084002.

- [19] K.C.B. New, D. Choi, J.M. Centrella, P. MacNeice, M.F. Huq, K. Olson, Three-dimensional adaptive evolution of gravitational waves in numerical relativity, *Phys. Rev. D* 62 (2000) 084039.
- [20] E. Schnetter, S.H. Hawley, I. Hawke, Evolutions in 3D numerical relativity using fixed mesh refinement, *Class. Quant. Grav.* 21 (2004) 1465.
- [21] B. Imbiriba et al., Evolving a puncture black hole with fixed mesh refinement, *Phys. Rev. D* 70 (2004) 124025.
- [22] F. Pretorius, Numerical relativity using a generalized harmonic decomposition, *Class. Quant. Grav.* 22 (2005) 425.
- [23] P. Diener, N. Jansen, A. Khokhlov, I. Novikov, Adaptive mesh refinement approach to construction of initial data for black hole collisions, *Class. Quant. Grav.* 17 (2000) 435.
- [24] J.D. Brown, L.L. Lowe, Distorted black hole initial data using the puncture method, *Phys. Rev. D* 70 (2004) 124014.
- [25] J.D. Brown, L.L. Lowe, Multigrid elliptic equation solver with adaptive mesh refinement, *J. Comp. Phys.* 209 (2005) 582.
- [26] F. Pretorius, Evolution of binary black hole spacetimes, *gr-qc/0507014*, 2005.
- [27] C.W. Misner, K.S. Thorne, J.A. Wheeler, *Gravitation*, W.H. Freeman and Company, New York, 1973.
- [28] R. Arnowitt, S. Deser, C.W. Misner, in: L. Witten (Ed.), *Gravitation: An Introduction to Current Research*, Wiley, New York, 1962.
- [29] T. Piran, Numerical codes for cylindrical relativistic systems, *J. Comp. Phys.* 35 (1980) 254.
- [30] M.W. Choptuik, Consistency of finite difference solutions of Einstein's equations, *Phys. Rev. D* 44 (1991) 3124; *Gravitation*, W.H. Freeman and Company, New York, 1973.
- [31] A.S. Almgren, J.B. Bell, P. Colella, L.H. Howell, M.L. Welcome, A conservative adaptive projection method for the variable density incompressible Navier–Stokes equations, *J. Comput. Phys.* 142 (1998) 1.
- [32] M.W. Choptuik, E.W. Hirschmann, S.L. Liebling, F. Pretorius, An axisymmetric gravitational collapse code, *Class. Quant. Grav.* 20 (2003) 1857.
- [33] L. Lindblom, M.A. Scheel, Energy norms and the stability of the Einstein evolution equations, *Phys. Rev. D* 66 (2002) 084014.
- [34] H. Shinkai, G. Yoneda, Re-formulating the Einstein equations for stable numerical simulations: formulation problem in numerical relativity, *gr-qc/0209111*.
- [35] M. Anderson, R.A. Matzner, Extended lifetime in computational evolution of isolated black holes, *gr-qc/0307055*.
- [36] R.A. Matzner, Hyperbolicity and constrained evolution in linearized gravity, *Phys. Rev. D* 71 (2005) 024011.
- [37] M. Holst, L. Lindblom, R. Owen, H.P. Pfeiffer, M.A. Scheel, Lawrence E. Kidder, Optimal constraint projection for hyperbolic evolution systems, *Phys. Rev. D* 70 (2004) 084017.
- [38] S. Bonazzola, E.ourgoulhon, P. Grandclement, J. Novak, A constrained scheme for Einstein equations based on Dirac gauge and spherical coordinates, *Phys. Rev. D* 70 (2004) 104007.
- [39] J.W. York, in: L. Smarr (Ed.), *Sources of Gravitational Radiation*, Cambridge University Press, Seattle, 1978.
- [40] H.P. Pfeiffer, L.E. Kidder, M.A. Scheel, S.A. Teukolsky, A multidomain spectral method for solving elliptic equations, *Comput. Phys. Commun.* 152 (2003) 253.
- [41] F. Pretorius, L. Lehner, Adaptive mesh refinement for characteristic codes, *J. Comp. Phys.* 198 (2004) 10.
- [42] M.J. Berger, J. Olinger, Adaptive mesh refinement for hyperbolic partial differential equations, *J. Comp. Phys.* 53 (1984) 484.
- [43] F. Pretorius, Numerical Simulations of Gravitational Collapse, University of British Columbia, Ph.D. thesis, 2002.
- [44] H. Kreiss, J. Olinger, Methods for the approximate solution of time dependent problems, Global Atmospheric Research Programme, Publications Series No. 10, 1973.
- [45] R.L. Marsa, M.W. Choptuik, The RNPL User's Guide, 1995. Available from: http://laplace.physics.ubc.ca/Members/marsa/rnpl/users_guide/users_guide.html.
- [46] A. Brandt, Multi-level adaptive solutions to boundary-value problems, *Math. Comput.* 31 (1977) 330.
- [47] U. Trottenberg, C. Oosterlee, A. Schuller, *Multigrid*, Academic Press, London, 2001.
- [48] M.W. Choptuik, A Study of Numerical Techniques for the Initial Value Problem in General Relativity, University of British Columbia, M.Sc. thesis, 1982.
- [49] M.W. Choptuik, W.G. Unruh, An introduction to the multi-grid method for numerical relativists, *Gen. Relat. Grav.* 18 (1986) 813.
- [50] J. Bardeen, T. Piran, General relativistic axisymmetric rotating systems: coordinates and equations, *Phys. Rep.* 96 (1983) 205.
- [51] R.F. Stark, T. Piran, Gravitational-wave emission from rotating gravitational collapse, *Phys. Rev. Lett.* 55 (1985) 891.
- [52] C.R. Evans, in: J. Centrella (Ed.), *Dynamical Spacetimes and Numerical Relativity*, Cambridge University Press, Cambridge, 1986.
- [53] T. Nakamura, K. Oohara, Y. Kojima, General relativistic collapse of axially symmetric stars, *Prog. Theor. Phys. Suppl.* 90 (1987) 13.
- [54] C.R. Evans, in: C.R. Evans, L.S. Finn, D.W. Hoboll (Eds.), *Frontiers in Numerical Relativity*, Cambridge University Press, Cambridge, 1989.
- [55] S.L. Shapiro, S.A. Teukolsky, Formation of naked singularities: the violation of cosmic censorship, *Phys. Rev. Lett.* 66 (1991) 994.
- [56] A.M. Abrahams, C.R. Evans, Trapping a geon: black hole formation by an imploding gravitational wave, *Phys. Rev. D* 46 (1992) R4117.
- [57] A.M. Abrahams, C.R. Evans, Critical behavior and scaling in vacuum axisymmetric gravitational collapse, *Phys. Rev. Lett.* 70 (1993) 2980.
- [58] A.M. Abrahams, G.B. Cook, S.L. Shapiro, S.A. Teukolsky, Solving Einstein's equations for rotating spacetimes: evolution of relativistic star clusters, *Phys. Rev. D* 49 (1994) 5153.
- [59] G.B. Cook, S.L. Shapiro, S.A. Teukolsky, Testing a simplified version of Einstein's equations for numerical relativity, *Phys. Rev. D* 53 (1996) 5533.
- [60] H. Dimmelmeier, J.A. Font, E. Mueller, Relativistic simulations of rotational core collapse. I. Methods, initial models, and code tests, *Astron. Astrophys.* 388 (2002) 917.
- [61] D. Garfinkle, G.C. Duncan, Numerical evolution of Brill waves, *Phys. Rev. D* 63 (2001) 044011.

- [62] I. Olabarrieta, M.W. Choptuik, Critical phenomena at the threshold of black hole formation for collisionless matter in spherical symmetry, *Phys. Rev. D* 65 (2002) 024007.
- [63] J.F. Ventrella, M.W. Choptuik, Critical phenomena in the Einstein-Massless-Dirac system, *Phys. Rev. D* 68 (2003) 044020.
- [64] L. Andersson, V. Moncrief, Elliptic-hyperbolic systems and the Einstein equations, *Annales Henri Poincaré* 4 (2003) 1.
- [65] S.F. McCormick, J. Thomas, *Math. Comput.* 46 (1986) 439.
- [66] D. Choi, Private Communication.
- [67] M.J. Berger, I. Rigoutsos, An algorithm for point clustering and grid generation, *IEEE Trans.* 21 (5) (1991).